

Statistics of Geomagnetic Storms: Global Simulations Perspective

Tuija I. Pulkkinen 1,*, Austin Brenner 2, Qusai Al Shidi 1 and Gabor Toth 1

¹Department of Climate and Space Sciences and Engineering, University of Michigan, Ann Arbor, MI

²Department of Aerospace Engineering, University of Michigan, Ann Arbor, MI

Correspondence*: Corresponding Author tuija@umich.edu

2 ABSTRACT

- We present results of 131 geomagnetic storm simulations using the University of Michigan 3 Space Weather Modeling Framework Geospace configuration. We compare the geomagnetic indices derived from the simulation with those observed, and use 2D cuts in the noon-midnight planes to compare the magnetopause locations with empirical models. We identify the location of the current sheet center and look at the plasma parameters to deduce tail dynamics. We show 7 that the simulation produces geomagnetic index distributions similar to those observed, and that their relationship to the solar wind driver is similar to that observed. While the magnitudes of the Dst and polar cap potentials are close to those observed, the simulated AL index is consistently 10 underestimated. Analysis of the magnetopause position reveals that the subsolar position agrees 11 well with an empirical model, but that the tail flaring in the simulation is much smaller than that in the empirical model. The magnetotail and ring currents are closely correlated with the Dst index, 14 and reveal a strong contribution of the tail current beyond 8 R_E to the Dst index during the storm main phase.
- 16 Keywords: Space Weather, Geomagnetic Storms, Solar Wind Magnetosphere Coupling, Global Simulations, Magnetic Reconnection

1 INTRODUCTION

- 17 Geomagnetic storms are a class of major disturbances in the Earth's space environment driven by solar
- 18 wind structures containing either strong southward interplanetary magnetic field (IMF), large solar wind
- 19 speed or both (Gonzalez et al., 1994). The storm intensity is measured by the Dst index, and storms are
- 20 often classified to minor storms causing a magnetic depression of the Earth's field by more than -50 nT
- 21 and major storms with Dst peak below -100 nT (Burton et al., 1975). Other indicators of stormtime activity
- 22 include an enhanced cross-polar cap potential (CPCP) and strong auroral electrojet currents causing large
- 23 signals in the AL index (Davis and Sugiura, 1966).
- 24 The relationship between the solar wind driver and the consequent geomagnetic activity is complex, and
- 25 often expressed in terms of coupling functions that relate interplanetary parameters with the geomagnetic
- 26 indices. Coupling functions have been widely used and much studied (see e.g. Borovsky and Birn, 2014;
- 27 Lockwood, 2019, 2022). On one hand, the coupling functions describe different attributes of the driver
- 28 such as the solar wind electric field (Burton et al., 1975), the incident Poynting flux (Akasofu, 1981) or
- 29 the reconnected magnetic flux (Newell et al., 2007) at the magnetopause. On the other hand, they have

been optimized to different geomagnetic indices like Dst (Akasofu, 1981), the AL index (McPherron

- 31 et al., 2015), or cross-polar cap potential (Lockwood and McWilliams, 2021). The coupling functions
- 32 are typically derived using theoretical considerations together with correlations between the solar wind
- 33 parameters and geomagnetic indices.
- 34 The lack of global observations either in space or on ground brings inherent limitations to correlation
- 35 studies between the interplanetary parameters and geomagnetic indices. Scatter sources include but are not
- 36 limited to errors in measurements and transit time of the solar wind and IMF (Papitashvili et al., 2014),
- 37 dynamics occurring at the bow shock and within the magnetosheath (Pulkkinen et al., 2016), and lack
- 38 of station coverage and signals in ground magnetic recordings caused by ground conductivity structure
- 39 and other effects not related to the solar wind driving (Häkkinen et al., 2002; Tanskanen et al., 2001).
- 40 Furthermore, the magnetospheric response to the solar wind driver is neither instantaneous nor independent
- 41 of the state of the magnetosphere (Pulkkinen et al., 2006b; Brenner et al., 2021).
- 42 Global MHD simulations can model the solar wind magnetosphere coupling covering the entire
- 43 magnetosphere out to cislunar distances (e.g. Janhunen et al., 2012; Tóth et al., 2012). Such simulations
- 44 have been shown to give an accurate representation of the large-scale evolution of the magnetosphere-
- 45 ionosphere system (Liemohn et al., 2018), while allowing us to quantitatively assess the plasma and energy
- 46 flow from the solar wind into the magnetosphere (Palmroth et al., 2003), and thereby assess the parameters
- 47 controlling the coupling.
- 48 Using methods developed in Palmroth et al. (2003), Pulkkinen et al. (2008) examined the energy input
- 49 from the solar wind into the magnetosphere-ionosphere system under a variety of driving conditions
- 50 (northward and southward IMF, high and low solar wind density and speed) in the GUMICS-4 global MHD
- 51 simulation (Janhunen et al., 2012). They showed that the reconnection efficiency is higher for high solar
- 52 wind speed, and that the optimal energy coupling function scaled as the electric field parallel to the large-
- 53 scale X-line at the magnetopause (i.e., proportional to $\sin \theta$ rather than the often-used $\sin \theta/2$). Furthermore,
- 54 the response of the magnetopause energy transfer depends on the past history with energy input being
- 55 larger for periods with large preceding energy input Palmroth et al. (2006); Pulkkinen et al. (2006a). Using
- similar methodology, Wang et al. (2014) examined the energy transfer through the magnetopause in the Hu
- 57 et al. (2005) simulation. They arrived at a new coupling function proportional to the energy incident at the
- 58 magnetopause, which gave better correlations with geomagnetic indices than the Akasofu (1981) epsilon
- 59 function. Both of these studies suffer from the limitation of using pure MHD plasma description, which
- 60 does not allow for development of a high-energy ring current in the inner magnetosphere that is a major
- 61 characteristic of a magnetic storm evolution.
- The cross-polar cap potential is a measure of the coupling between the ionosphere and the solar wind: The
- 63 rate at which magnetic flux reconnects at the magnetopause is equal to a voltage drop along the reconnection
- 64 X-line. This potential maps to the ionosphere along the magnetic field lines, and can be measured as the
- 65 cross-polar cap potential (Crooker, 1988; Siscoe et al., 2002). However, this direct relationship is altered
- as other factors contribute to the CPCP. A residual potential exists even if the dayside reconnection is
- 67 completely shut off (Axford and Hines, 1961), and the potential saturates at high levels of driving (Russell
- 68 et al., 2001). The saturation potential value varies from study to study, but several authors have linked the
- 69 process to low Mach number conditions in the solar wind (Lopez et al., 2010; Myllys et al., 2017; Lakka
- 70 et al., 2018), typical of Interplanetary Coronal Mass Ejections (ICME) that are key drivers of geomagnetic
- 71 storms (Kilpua et al., 2017).

In this paper, we return to the analysis of geomagnetic storms and their drivers using the SWMF Geospace

- 73 model. Improving on the simulation studies referenced above, we include the ring current formation, which
- 74 requires coupling the MHD code with a model for the drift physics processes in the inner magnetosphere
- 75 (De Zeeuw et al., 2004), and which is critical in getting a realistic representation of the storm evolution
- 76 (Liemohn et al., 2018).

77 We examine a statistical dataset of geomagnetic storm simulations. We compare and contrast the simulated

- 78 values with those observed in order to discuss the performance of the coupling parameters and the dynamics
- 79 of the solar wind magnetosphere coupling. Section 2 introduces the model, section 3 presents the dataset,
- 80 section 4 discusses the model performance, section 5 compares the model and observed coupling function
- 81 correlations, section 6 examines the magnetotail configuration, and section 7 shows the comparison of the
- 82 model magnetopause location with an empirical formulation. Section 8 concludes with discussion.

2 SPACE WEATHER MODELING FRAMEWORK

- 83 The Space Weather Modeling Framework (SWMF) comprises a set numerical models to simulate plasma
- 84 processes from the Sun to Earth's upper atmosphere and/or the outer heliosphere (Tóth et al., 2012;
- 85 Gombosi et al., 2021). The simulation core is the Block-Adaptive-Tree-Solarwind-Roe-Upwind-Scheme
- 86 (BATSRUS), which solves the 3-dimensional extended magnetohydrodynamic (MHD) equations in various
- 87 forms (Powell et al., 1999). In the Geospace configuration (see Figure 1) BATSRUS is coupled to the
- 88 Ridley Ionosphere electrodynamics Model (RIM, Ridley et al. (2004)) as well as to the Rice Convection
- 89 Model (RCM), a drift physics model for the inner magnetosphere ring current (Wolf, 1983). The Geospace
- 90 configuration used in this study is similar to the one operationally used at the NOAA Space Weather
- 91 Prediction Center (SWPC), and has been extensively tested and validated for numerical stability and
- 92 robustness (Kwagala et al., 2020).
- 93 BATSRUS, configured to solve the semi-relativistic MHD equations, models the solar wind and the
- magnetosphere with an adaptive grid resolution ranging from $0.125 R_E$ in the near-Earth region to $8R_E$
- 95 in the distant tail. The simulation box covers the region from $32 R_E$ to $-224 R_E$ in the X direction and
- 96 $\pm 128 R_E$ in the Y and Z directions in Geocentric Solar Magnetospheric (GSM) coordinates. The inner
- 97 boundary is a spherical surface at radial distance $R = 2.5 R_E$. The Geospace setup uses the ideal MHD
- 98 equations to describe the large-scale plasma dynamics in the solar wind and magnetosphere. The adaptive
- 99 grid is fixed in time, selected to focus the highest resolution to close to the dayside boundaries and to the
- 100 magnetotail where many of the smaller scale dynamic processes take place.
- The Ridley Ionosphere electrodynamics Model (RIM) solves the Poisson equation for the electrostatic
- 102 potential on a two-dimensional height-integrated ionospheric surface (Ridley et al., 2004). BATSRUS
- 103 passes field-aligned currents from the simulation inner boundary to RIM, which uses them to derive the
- 104 ionospheric conductance distribution in combination with the background conductances from the solar
- illumination characterized with the F10.7 index. RIM solves the Vasyliunas (1970) equation for the electric
- 106 potential, and feeds the electric field back to BATSRUS to drive the inner boundary condition for the
- 107 plasma velocity. RIM and BATSRUS are coupled at every 5 seconds.
- The non-Maxwellian plasmas in the inner magnetosphere are modeled by the Rice Convection Model
- 109 (RCM) that solves the bounce- and pitch-angle-averaged phase space densities for protons, singly charged
- oxygen, and electrons (Toffoletto et al., 2003). BATSRUS feeds the outer boundary condition and magnetic
- 111 field configuration and RIM feeds the $E \times B$ drift speed to RCM. The RCM plasma density and pressure
- 112 values are returned to BATSRUS, which relaxes MHD values towards the RCM values with a 20 s relaxation

- time (De Zeeuw et al., 2004). The 2-way coupling of BATSRUS with RCM and the one-way coupling of
- 114 RIM to RCM are performed every 10 seconds.
- 115 This configuration can represent the dynamic response of the magnetosphere and ionosphere to the strong
- solar wind driving during geomagnetic storms. The RCM facilitates development of strong ring current
- 117 (Liemohn et al., 2018), and the ground magnetic disturbances can be computed by Biot-Savart integration
- of the currents external to the Earth, using both the MHD and RIM domains (Yu and Ridley, 2008).
- 119 The Geospace model takes the solar wind plasma parameters (density, temperature, velocity, magnetic
- 120 field), the F10.7 radio flux, and the dipole orientation as function of time as input and boundary conditions,
- and develops the magnetosphere from an empty dipole subjected to the observed solar wind which is fed in
- 122 to the Sunward boundary of the simulation box.
- The SWMF and the Geospace configuration numerical schemes are described in detail in Tóth et al.
- 124 (2012); Pulkkinen et al. (2013); Gombosi et al. (2021)

Figure 1. The SWMF Geospace model setup. The arrays indicate the one-way or two-way couplings between the modules (see text). The orange boxes indicate model input parameters.

3 STATISTICAL ANALYSIS OF GEOMAGNETIC STORMS

- We study a set of 131 geomagnetic storms with Dst minima below -50 nT identified from the time period
- 126 2010–2019 (Al Shidi et al., 2022). Each of the storms was run with the SWMF Geospace model described
- 127 above, using the same model setup apart from the initial and boundary conditions given by the solar wind
- 128 parameters and the F10.7 solar flux. The model outputs comprised the geomagnetic indices as well as
- noon-midnight and equatorial plane cuts of the 3D magnetosphere domain. Each of the storms was run
- 130 from 6 hours prior to onset for 54 hours. While the ionospheric and geomagnetic index data was stored at
- 131 1-min intervals, the 2D magnetospheric output was saved at 15-min cadence.
- Figures 2 3, and 4 show results from a sample storm that took place on March 16-17, 2015, and introduce
- 133 the type of simulation results used in the following analysis. Figure 2 shows simulation results in the
- 134 noon-midnight meridian plane with magnetopause identifications overlaid (see below).
- Figure 3 shows the observed solar wind and IMF parameters as well as the geomagnetic indices compared
- 136 with the simulation results shown in light blue. The storm main and recovery phases are indicated by the
- darker and lighter gray shading, respectively. The storm main phase is driven by strongly southward IMF
- 138 as well as high-speed solar wind. The polar cap potential was of the order of 150 kV during the main
- phase, and the observed AL index reached below -1,500 nT. Characteristically to the SWMF Geospace
- 140 simulation, the simulation AL does not reach such low values. However, the bottom panel shows the Dst
- index, which is highly correlated with that derived from the simulation.
- The left panels of Figure 4 show the magnetospheric tail magnetic field, electric current, and plasma
- 143 velocity along the tail current sheet center in the midnight meridian in a keogram format. The higher
- values of the magnetic field in the magnetotail are characteristics of tail field dipolarizations. The strong
- 145 current in the inner tail represents the intensifying ring current during the storm main phase. The flow
- speed shows both tailward and Earthward flow periods here it is especially important to remember that
- 147 the noon-midnight meridian represents only one location in the tail, while the flows are highly structured in
- 148 the cross-tail dimension.

The right panels show the magnetopause locations, ring and tail current intensities, and the integrated magnetotail flux. Note the compression of the magnetospheric size during the storm main phase, and the high level of correlation between the tail and ring currents. More detailed description of each of the parameters will be provided in later sections.

149

150

151

152

162

163

164

165

Figure 2. Noon-midnight meridian cuts from the simulation. (Top left) Plasma density in cm⁻³; (Top right) Plasma velocity V_X component in km/s; (Bottom left) Current density in μ A/m²; and (Bottom right) β^* parameter (see text). The white lines show the $\beta^* = 0.7$ contours, which are used to define the simulation magnetopause location. The black thick curve shows the Shue magnetopause model (see text).

Figure 3. (Left panel) Solar wind driver parameters: (Top) IMF B_Z in nT; (Middle) solar wind speed in km/s; and (Bottom) Newell coupling function (arbitrary units, see text). (Right panel) Geomagnetic index response: (Top) Cross-polar cap potential in kV; (Middle) Auroral electrojet AL index in nT; and (Bottom) Storm Dst index in nT. The observed valueas are shown in dark blue, the SWMF simulation values in light blue. Storm main phase (from start of Dst decrease to peak Dst) and recovery phase (from peak Dst to storm end) are shown with darker and lighter gray shading, respectively.

Figure 4. (Left panel) Simulation results along the magnetotail current sheet at the midnight meridian in a keogram format (see text for definition of the current sheet surface): (Top) Tail B_Z in nT; (Middle) Z-integrated current intensity (arbitrary units, see text) with current peak intensity location shown with the black dotted line; (Bottom) Plasma velocity V_X component in km/s. The storm main phase and recovery phases are defined by the dotted lines. (Right panel) Characteristic numbers for the magnetospheric state: (Top) Magnetopause nose at Y=Z=0 and magnetopause distance from the X-axis at Y=0, $X=-10R_E$. The Shue model is shown in dark blue, the SWMF Geospace values are shown in lighter blue. The southern lobe simulation value is shown with the lightest shade of blue; the Shue model is symmetric and gives the same value for northern and southern lobes. (Middle) Total ring current (orange) and tail current (dark red) integrated along the tail length in MA (see text); (Bottom) Closed magnetic flux through the magnetotail at midnight meridian (arbitrary units, see text). Storm main phase (from onset to peak Dst) and recovery phase (from peak Dst to storm end) are shown with darker and lighter gray shading, respectively.

For each storm, we identified onset time as the time when the Dst index starts to decrease (i.e., not 153 necessarily the time of impact of an interplanetary coronal mass ejection or ICME), a storm peak as the 154 time of the Dst minimum, and an end indicating recovery of the Dst index, a second major depression 155 of the Dst index indicating another period of main phase -like activity, or end of simulation period. Note 156 that while we wish to exclude main phase -like behavior from the analysis of recovery phase phenomena, 157 we recognize that individual storms can have complex structure with multiple activations. Note also that 158 many of the simulations do not reach to the end of the observed recovery phase. Furthermore, storms were 159 categorized into two groups, "major storms" with peak Dst below -100 nT and "minor storms" with Dst 160 peak between -50 and -100 nT, following often-used convention. 161

The full set of storms is represented in the form of a superposed epoch analysis. Figure 5 shows superposed epoch curves for the major (in red) and minor (in blue) storms with the standard deviation (orange/light blue shading) indicating the variability in each category. The superposition was done aligning the onset times, but time is not scaled to account for the main phase duration. The top row shows the ring current

(Dst) index, the middle row the auroral electrojet (AL) index, and the bottom row shows the cross-polar cap

- potential (CPCP) from the northern hemisphere. The left column shows the observed indices extracted from
- the OMNI database (https://omniweb.nasa.gov); the CPCP values are computed using the formulation
- 169 from Ridley et al. (2004) as a function of the polar cap index (PCI) measured in the northern polar cap
- 170 (Thule station) and season as

$$CPCP = 29.28 - 3.31\sin(T + 1.49) + 17.81PCI \tag{1}$$

- where the time of year is scaled as $T = 2\pi (N_{MONTH}/12)$ and the numbering of months starts from zero
- (Jan = 0). The middle column shows the simulated values, while the right column show the difference
- between the simulated and observed values, i.e., the model error and its variance.
- 174 The simulations of the major and minor storms give quite good prediction of the Dst index, with relatively
- moderate errors between the model and observed values. The errors are closest to zero during the storm
- 176 start and main phase, while they systematically increase (more for the major storms) during the recovery
- 177 phase. This indicates that the Geospace model has a tendency to predict smaller Dst disturbance during the
- 178 recovery phase, i.e., recover faster than the observed Dst.
- 179 The AL index has large variability in observations, while the values and the variability are much smaller
- 180 in the simulation. Consequently, the errors are large with no systematic trend during the storm for minor
- 181 storms, but a tendency for larger errors during the storm main phase than during the recovery phase for
- 182 major storms. For strong AL activity, the Geospace model AL indices are substantially weaker than the
- 183 observed ones. Furthermore, as accurate modeling of individual substorms still poses a major challenge to
- 184 the simulations, the timing differences in the substorm evolution cause large instantaneous errors in the
- 185 observed and model values.
- The simulated polar cap potentials are somewhat larger than those obtained from the empirical model, and
- 187 furthermore show a larger difference between the averages of the major and minor storms. The errors are
- largest during the main phase, while close to zero during the recovery phase. This means that the simulation
- 189 predicts larger polar cap potentials than the empirical model, indicative of either stronger dayside merging
- 190 or weaker tail reconnection during the storm main phase.

Figure 5. (Top row) Dst; (Middle row) AL; and (Bottom row) CPCP from (Left column) Observations; (Middle column) Simulation; and (Right column) Error (simulation – observation) for minor (blue, peak Dst > -100 nT) and major (red, peak Dst < -100 nT) storms. The thick solid lines show the superposed epoch curve (1-min temporal resolution), the shadings indicate the standard deviation.

4 MODEL PERFORMANCE

- 191 The model performance can be assessed by computing skill scores for the geomagnetic index predictions.
- 192 The Heidke skill score Heidke (1926) is one often used performance measure for geomagnetic index
- 193 predictions, and is defined as

$$HSS = \frac{2(H \cdot N - M \cdot F)}{(H+M)(M+N) + (H+F)(F+N)},$$
(2)

where H = hit, M = miss, F = false positive, and N = true negative, which are evaluated based on the observation and prediction values being above or below the selected thresholds. The HSS maximum value 195

- for no misses and no false positives is 1, value of zero indicates no skill, and negative values indicate skill 196
- worse than chance coincidence. 197
- Figure 6 shows heat map plots of hourly averaged index values for Dst, AL, and the polar cap potential, 198
- as well as the errors as function of the observed index values (right column). The left and middle column 199
- show the major and minor storms separately. The dotted lines indicate the chosen "event" values for the 200
- Heidke skill score calculation (-50 nT for Dst, -150 nT for AL, and 80 kV for the CPCP). While changing 201
- the selected "event" values somewhat changes the skill scores, our conclusions are independent of the exact 202
- 203 values of the limits.
- The Heidke skill score for the major storms is HSS = 0.61, which is somewhat better than the value 0.57 204
- obtained by Liemohn et al. (2018), who computed skill scores for a 3-month period including both storm 205
- and nonstorm times. The skill for the smaller storms is lower (0.48). Furthermore, the skill scores for the 206
- AL and the CPCP are lower, showing similar difference between major and minor storms. Comparison 207
- between minor and major storms and with the Liemohn et al. (2018) results indicate that the Heidke skill 208
- scores are larger for data sets that contain sufficient number of data points in the "hit" quadrant. 209
- 210 The plots also indicate the values of the commonly used Pearson linear correlation coefficient defined as
- the ratio of the covariance and the product of the standard deviations of each set (o = observation, m =211
- 212 model:

$$R = \frac{\sigma_{mo}}{\sigma_m \sigma_o} \tag{3}$$

- where the covariance is given by $\sum_i (m_i \langle m \rangle)(o_i \langle o \rangle)/(N-1)$ and the variance (square of the standard deviation) is given by $\sum_i (x_i \langle x \rangle)^2/(N-1)$, and $\langle x \rangle = \sum_i x_i/N$ denotes the mean for
- 214
- 215 x = m, o.
- The right column shows the errors (simulation observation) as function of the observed values. All errors 216
- show a tendency to increase with increasing level of activity, but for Dst and CPCP, the effect is relatively 217
- 218 minor. On the other hand, the error in AL is strongly and almost linearly dependent on the intensity of
- the AL index throughout the higher values of the observed AL. This indicates that the simulation value is 219
- smaller than the predicted value by a factor dependent on the intensity of the (observed) activity. While the 220
- scatter in the values is still large, the model predictive performance could be improved by accounting for 221
- 222 this persistent behavior.

Figure 6. Scatter plots showing hourly values of (Top row) Dst; (Middle row) AL; and (Bottom row) the CPCP observed vs. simulated values, for (Right column) major storms and (Center column) minor storms. The unity line is shown in thin solid line, the dotted lines show the threshold values used in the Heidke Skill Score (HSS) calculation (see text). (Right column) Errors (simulated – observed value) as function of the observed values. The magenta dots show bin averages, and the vertical thin lines indicate the standard deviation in each bin.

SOLAR WIND DRIVER

Most geomagnetic activity predictions rely on empirical relationship between the driving solar wind and 223 interplanetary magnetic field and the resulting geomagnetic activity. The Newell et al. (2007) coupling

function, representing the rate of change of magnetic flux at the nose of the magnetopause, is given by

$$\frac{d\Phi_{MP}}{dt} = \alpha \left[V^2 B_T \sin^4 \left(\frac{\theta}{2} \right) \right]^{2/3} \tag{4}$$

- where $\theta = \tan^{-1}(B_Y/B_Z)$ is the IMF clock angle and $B_T = (B_Y^2 + B_Z^2)^{1/2}$ denotes the transverse
- component of the magnetic field perpendicular to the Sun-Earth line. While a normalizing factor $\alpha \sim 10^3$ is
- 228 needed to get the coupling function in units of Wb/s, here we show the coupling intensity as unnormalized
- 229 ($\alpha = 1$) and thus in arbitrary units.
- Figure 7 shows the geomagnetic indices as function of the Newell coupling function separately for the
- 231 main phase and recovery phases for all storms. The data are averaged to 1-hour bins, which should remove
- 232 most scatter associated with timing errors of the arrival time of the solar wind front at the subsolar bow
- 233 shock. Correlations are shown both for observations (dark purple) and simulation results (magenta). The
- 234 correlations don't show significant differences between the main and recovery phases, but the scatter during
- 235 the recovery phase is somewhat smaller.
- 236 Essentially, the distribution of points for the observations and the simulation look similar. This indicates
- 237 that the simulation is doing as good a job in the prediction as the observations. On the other hand, despite
- 238 the simulation being deterministic, it does not provide better correlations. This fact emphasizes that better
- 239 observations will not lead to improved correlations (as the simulation can use data from any point), and
- 240 that improving the predictions requires better coupling functions (with inclusion of time history of the solar
- 241 wind driver and magnetospheric state).

Figure 7. (Top row) Dst; (Middle row) AL; and (Bottom row) CPCP during (Left column) the storm main phase and (Right column) recovery phase as function of the Newell coupling function (in arbitrary units) using 1-hour averaged data for observations (dark blue) and simulations (light blue).

6 MAGNETOTAIL CONFIGURATION

- 242 Using two-dimensional cuts in the simulation saved at 15-min cadence, we examine the properties at the
- 243 center of the current sheet along the midnight meridian. The current sheet center is defined as the point with
- 244 minimum B_X between the lobes for each X-value along the tail, which in a simple geometry coincides with
- 245 the peak of the current intensity. At times, the current sheet is bifurcated tailward of a large-scale neutral
- 246 line. In such cases, the algorithm chooses one or the other branches and uses those values as the current
- 247 sheet center. This choice does not significantly impact our results that focus on the inner magnetosphere.
- For each storm and each time step, we identify the current sheet center location Z_{CS} along the midnight
- 249 meridian, plasma velocity V_X , magnetic field B_Z , and current j_Y at the current sheet center, and integrate
- 250 the total current $(J_Y(X) = \int j_Y dZ)$ across the current sheet thickness. We extend the analysis out to
- 251 $X = -20R_E$.
- Furthermore, we identify the location of the innermost X-line, X_{NL} , from a B_Z sign change, and
- 253 calculate the amount of closed magnetic flux through the tail from

$$\Phi_C = \int_{X_{NL}}^{-3R_E} B_Z dX \tag{5}$$

where the limit at $-3R_E$ is close to the inner boundary of the simulation domain. As the analysis is limited to $X > -20R_E$, for situations where the X-line is further than that, we set $X_{NL} = -20R_E$ (the flux 255 crossing the equatorial plane beyond that distance is small and would not cause significant changes to the 256 results). Furthermore, as the magnetic flux is generally defined as magnetic field through an area, and we 257 are limited here to the two-dimensional noon-midnight plane (i.e. flux per unit cross-tail width), we show 258 the closed flux in arbitrary units focusing on time variations rather than absolute values. 259

260

261

262 263

278

279

280

281

282

283

While the distinction between tail and ring current is arbitrary as well in observations as in the simulation, we denote the current inside of 8 R_E as the "ring current" and the current tailward of 8 R_E as "tail current". Similarly to the magnetic flux, we integrate the total ring and tail currents crossing the midnight meridian

$$I_{RING} = \int_{-8R_E}^{-3R_E} J_Y(X)dX$$

$$I_{TAIL} = \int_{-20R_E}^{-8R_E} J_Y(X)dX.$$
(6)

$$I_{TAIL} = \int_{-20R_E}^{-8R_E} J_Y(X) dX.$$
 (7)

Figure 8 shows the relationship of the ring current, tail current, and closed flux with the Dst index and 264 the cross-polar cap potential. The good correlation between the ring current and the Dst index shows that, 265 indeed, the Dst index is a good (albeit not strictly linear) measure of the ring current. The ring current 266 intensity for the same value of Dst is higher during the main phase than during the recovery phase, which 267 likely comes from the positive contribution to Dst from the dayside compression, which is often larger 268 during the main phase than during the recovery phase. The amount of closed flux along the midnight 269 meridian is likewise well correlated with Dst, linking the decrease of tail magnetic flux to the intensification 270 of the ring (and tail) currents. 271

272 The tail current shows a larger variability, but still clear correlation with the Dst index, indicating that the currents even beyond $-8R_E$ contribute to the index in a significant way. 273

As the polar cap potential is quite directly driven by the changing solar wind driver, correlations with the 274 CPCP indicate directly driven processes. It is evident that the ring current is more directly driven (i.e. has 275 better correlation with the CPCP than the tail current, or the closed magnetic flux, that shows very low if 276 any correlation with the polar cap potential). 277

Figure 8. (Top row) Dst and (Bottom row) CPCP from the SWMF simulation as function of (Left column) total ring current; (Middle column) total tail current; and (Right column) Closed magnetic flux in the tail. The storm main phase (dark blue) and recovery phase (light blue) are shown separately. The data are snapshots taken at 15-min cadence in the magnetotail, tagged with the 30-min smoothed values of the indices.

Figure 9 shows the ring current, closed magnetic flux, Dst, and CPCP from the simulation as function of the Newell coupling parameter. The coupling parameter was smoothed by a 30-min filter before tagging the values to the simulation values. If the coupling parameter was a perfect indicator of the state of the magnetosphere, one would expect a very high correlation, as the simulation itself is a self-consistent, fully deterministic system. If the coupling function is not a perfect predictor of the ring current, there are other factors than those included in the coupling function that affect the state of the ring current. As can be seen

in the figure, the scatter in these parameters is large, indicative of the complexity of the processes and the significance of prior history both of the driver and of the magnetospheric dynamics not included in a point-by-point correlations. This complexity of course reflects on the scatter between the driver function and the geomagnetic indices discussed above. This conclusion remains valid even if we acknowledge that the simulation is not a perfect model of the true magnetospheric plasma system.

The coupling function comparison between the storm main and recovery phases is an indicator of the effects of time history to the correlations. The ring current intensity for similar level of driving is slightly higher for the recovery phase (likely indicating a higher preceding values of the current). Comparing to the Dst index, the difference is even more significant, highlighting the effects of the dayside processes on the Dst index. For the closed flux and cross-polar potential there is no difference in the distributions during storm main and recovery phases (not shown).

Figure 9. (Top left) Total ring current; (Bottom left) closed flux (in arbitrary units); (Top right) the simulation Dst; and (Bottom right) the CPCP as function of Newell coupling function (in arbitrary units). The storm main phase (dark blue) and recovery phase (light blue) are shown separately. The data are snapshots taken at 15-min cadence in the magnetotail, tagged with the 30-min smoothed values of the driver intensity.

7 DAYSIDE BOUNDARY LOCATIONS

289

290

291

292

293

294

303

304

305

306

307

309

310

The size of the magnetosphere is often characterized by the subsolar magnetopause location, which together with the flaring angle describes the shape of the boundary in the downwind direction. Statistical analyses yielded an empirical relationship (Shue et al., 1997), revised for extreme periods (Shue et al., 1998) to the form

$$R = R_0 \left[\frac{2}{1 + \cos(\theta)} \right]^{\alpha}, \tag{8}$$

$$R_0 = [10.22 + 1.29 \tanh (0.184(B_Z + 8.14))] P^{-1/6.6},$$
(9)

$$\alpha = (0.58 - 0.007B_Z) [1 + 0.24\ln(P)]. \tag{10}$$

The subsolar magnetopause nose distance from the Earth R_0 is given in R_E when the IMF B_Z is given in nT and the solar wind pressure P in nPa. The model assumes cylindrical symmetry, and produces a flaring magnetotail with the degree of flaring controlled by the factor α dependent on both IMF B_Z and dynamic pressure P.

We determined the magnetopause location from the 2D simulation cuts in the noon-midnight meridian plane using the open-closed field line boundary (in the dayside) and a parameter $\beta^* = 2\mu_0(P_{th} + P)/B^2$, which on the nightside shows a clear boundary between the dense magnetosheath with high $\beta^* > 1$ and the low-density, high-field magnetotail lobe with low $\beta^* << 1$ (see bottom left panel of Figure 2; Brenner et al., 2021). In determining the boundary location, we used a limit value of $\beta^* = 0.7$, but changing the limit value causes minimal changes to the outcome. Figure 2 shows the magnetopause definition overlaid with other parameters. This definition agrees with a velocity shear region at the high latitude tail magnetopause as well as follows closely the peak magnetopause currents.

311 Figure 2 also shows how the two magnetopause definitions agree during the storm main phase: The 312 subsolar locations are close to each other, but the Shue model flares much more than the magnetopause defined using the β^* parameter in the simulation. This is true more generally beyond the individual time 313 step shown here: Figure 4 shows time series for the subsolar point location as well as two individual points 314 at $X = -10R_E$ at the northern and southern tail lobes. While the subsolar locations agree for most of the 315 time, the magnetotail size in the SWMF is smaller than that predicted by the Shue model throughout the 316 317 storm with the exception of a short interval near the end of the main phase of the storm. Note also that the simulation magnetopause has a lot of small-scale variability, which is not always symmetric between the 318 319 northern and southern lobes, indicating that the internal magnetospheric dynamics and the changing dipole

- 320 tilt angle also contribute to the shape of the magnetopause.
- Figure 10 shows a statistical comparison of the subsolar and high-latitude $(Y = 0, X = -10R_E)$ tail magnetopause locations identified from the Geospace simulation and obtained from the Shue model using the formulation above. While there is a general correlation, there are clear deviations between the models.
- For the subsolar point, the models agree very well. However, generally the SWMF magnetopause values are slightly larger than the Shue model values. There are a few isolated occurrences where the SWMF values are considerably higher than those predicted by the Shue model. All of those occur during periods of very low solar wind density and moderate solar wind speed combined with negative IMF B_Z , and low Alfvén Mach numbers (< 4).
- The center and right panels show the magnetopause position at Y=0, $X=-10R_E$. At the high-latitude magnetotail, the magnetopause in SWMF is typically much closer to the Sun-Earth line than the Shue model for strongly driven conditions (smallest sizes of the magnetosphere). For more average driving conditions (and during the storm recovery phase), the difference diminishes, but the majority of Shue model values still fall below the Geospace ones.

Figure 10. SWMF magnetopause location vs. the Shue model. (Left) Magnetopause subsolar position X-value for Y=Z=0. (Middle) North lobe magnetopause position Z-value at Y=0, $X=-10R_E$. (Right) South lobe magnetopause position Z-value at Y=0, $X=-10R_E$.

334 Lastly we examine the magnetopause location dependence on the IMF driver parameters. Figure 11 shows the subsolar and north tail lobe locations as function of solar wind dynamic pressure and IMF B_Z 335 component. The black curves show the functional dependence of the Shue model (proportional to $P^{-1/6.6}$) 336 337 to guide the eye (not a fit to the points). It is clear that the functional dependence for the subsolar location 338 is similar for both the Shue model and the SWMF Geospace results, as the distributions almost completely overlap. However, for the tail lobe location, the functional form seems to still be valid for the SWMF 339 results (with large scatter), but the flaring angle formula, which also includes dynamic pressure, changes 340 341 that for the Shue model. Thus, the solar wind dynamic pressure response of the simulation differs from that 342 given by the Shue formulation, leading to less flaring tail and smaller tail lobe cross-sectional area.

The right panel of Figure 11 showing the tail lobe magnetopause dependence on the IMF B_Z documents that the magnetopause dependence on that parameter is at best weak. The largest magnetopause distances (largest flaring) is obtained when B_Z is close to zero, while both highly negative and highly positive IMF B_Z lead to compressed magnetosphere – much more so for the SWMF than for the Shue model.

Figure 11. Magnetopause location vs solar wind driver parameters. (Left) Magnetopause subsolar position X-value for Y = Z = 0 as function of solar wind dynamic pressure. (Middle) North lobe magnetopause position Z-value at Y = 0, $X = -10R_E$ as function of solar wind dynamic pressure. (Right) North lobe magnetopause position Z-value at Y = 0, $X = -10R_E$ as function of IMF B_Z . The Shue model values are shown in dark blue, the SWMF values are shown in light blue. The black lines show the Shue model functional dependence on dynamic pressure $(P^{-1/6.6})$.

8 DISCUSSION AND CONCLUSIONS

In this paper, we show results from the first large-scale statistical set of geomagnetic storm simulations developed by Al Shidi et al. (2022). We focus especially on comparing the geomagnetic indices with observed values as well as their dependence on the solar wind driver functions. While we did not have sufficient storage space to store all 3D simulation data, we focus on the 2D noon-midnight plane cuts and examine the magnetotail parameters along the tail current sheet center as well as the magnetopause locations at the dayside and in the magnetotail.

The statistical results can be used to infer the characteristic behavior of the SWMF Geospace simulation in a quantitative manner. All the examined indices (Dst, AL, CPCP) show behavior that is different during the storm main phase and recovery phase: For Dst, the error (simulated – observed value) is smallest during the main phase and increases systematically toward the recovery phase, while the opposite is true for the AL and CPCP. Thus, the model Dst index recovers faster than the observed one, indicating that further modeling or parametrization of the ring current decay processes could improve the model performance. Such processes could either be related to charge exchange and Coulomb collisions (Dessler and Parker, 1959; Fok et al., 1995) the wave-particle interactions scattering the ions away from the ring current Jordanova et al. (2001); Yue et al. (2019), multi-ion physics Daglis (2006) or ion outflow from the ionosphere Glocer et al. (2012). Regarding model performance metrics, the results in this paper, focusing solely on storm periods, are slightly better in terms of the HSS than those obtained by Liemohn et al. (2018), who used 3 months of real-time simulation containing both quiet and storm periods, but dominated by quiet periods.

The AL index shows a consistent offset from the observed value, which calls for further investigation of the auroral electrodynamics and magnetosphere – ionosphere coupling processes, including the acceleration region processes (Liemohn et al., 2002; Connor et al., 2016). Especially, the model has poor capability to reproduce the largest AL values, with the simulated values mostly limited to above –800 nT; the same is true for comparison with local magnetic perturbations Al Shidi et al. (2022). Furthermore, the instantaneous values of the AL index are critically dependent on timing of the substorm onsets and hence magnetotail dynamic processes, which still are difficult to reproduce to high accuracy in location and timing Newell et al. (2016); Maimaiti et al. (2019).

The auroral conductances regulate the closure of the field-aligned currents through the Hall and Pedersen currents in the ionosphere (Iijima and Potemra, 1976; Ridley et al., 2004). In general, auroral conductance arises from the solar EUV radiation in the dayside and from energetic particle precipitation to the auroral oval region especially in the nightside (Fuller-Rowell and Evans, 1987; Newell et al., 2009). In the SWMF simulation, the auroral conductances are derived from a simple empirical parametrization, which may in part lead to weaker coupling of the magnetotail currents into the ionosphere. Mukhopadhyay et al. (2020) examined the conductance effects on the coupling, and propose a new model for the auroral conductances, which has been coupled to the SWMF simulation. The CMEE model for auroral conductances allows for

a larger range of values, which lead to lower cross-polar potential values (as a result of currents closing between R1 and R2 currents), and larger ground magnetic perturbation values Mukhopadhyay et al. (2020) However, accurate modeling of both the diffuse and discrete sources and inclusion of their ionospheric impacts into the global simulations is still work in progress (Mukhopadhyay et al., 2022).

The polar cap potential is a central parameter describing the balance between dayside and nightside energy conversion processes, but observationally we are limited to radar (model-based) estimates of the convection (Koustov et al., 2009; Gao, 2012), low-Earth orbit satellite electric field measurements (Hairston et al., 1998), or empirical models based on the polar cap index Troshichev et al. (1996); Ridley et al. (2004). The Ridley et al. (2004) empirical model has quite high correlation with the simulated polar cap potential time series, with the simulation producing slightly higher potentials especially during the storm main phase. The Ridley et al. (2004) model based on the PCI is quite directly driven by the solar wind and IMF parameters, as is the simulation polar cap potential. Better global observations of the CPCP evolution are needed to fully understand the role of the detailed magnetospheric processes on the polar cap potential evolution.

The anticorrelation of the errors between the polar cap potential and the AL index indicates that the current closure processes between the ionosphere and the magnetosphere could be further optimized in the simulation. It seems that sometimes the magnetotail reconnection is not sufficiently strong to balance the dayside energy input, leading to weaker auroral currents (and hence AL) and stronger polar cap potential (larger lobe flux) Milan et al. (2003); Lockwood et al. (2009).

An important part of empirical predictions of the magnetospheric and ionospheric states is the use of coupling functions that tie the solar wind parameters to their geomagnetic response. For example, assuming that a solar wind coupling function is able to predict the ring current intensity, a deterministic simulation should always yield a good correlation. On the other hand, data contain many uncertainties: the solar wind input from L1 may be different than that impacting the Earth, and the Dst index is an indirect measure of the true ring current and may miss localized signatures. Therefore, even for a perfect coupling parameter, one would expect to have scatter in the results. Our results show that the distributions of the deterministic model and the observations are similar. This indicates that the scatter in the results arises largely from the inability of the simple coupling parameter to represent the complex solar wind – magnetosphere coupling and its time history, and that their predictive power cannot be further increased with a denser observational network. The magnetospheric processes as well as the time history of the system have quite strong effects on the system response, which yield high level of scatter in the correlation figures (see Figure 7, (Tsyganenko and Sitnov, 2005)). It also points out to the usefulness of a physics-based model over a prediction based on solar wind input only.

Analysis of the nightside ring current and tail current intensities shows that the ring current is highly correlated with the Dst index, but that there is a difference between the storm main and recovery phases. This likely stems from the dayside positive contribution to the Dst index, which is higher during the main phase. It is also noteworthy that the tail current and ring current intensities are highly correlated, and that they are of almost equal magnitude during the storm main phase, while the ring current starts to dominate during later phases of the storm, consistent with earlier observational and empirical model studies Ganushkina et al. (2005); Kalegaev and Makarenkov (2008). In our study, the "ring current" was arbitrarily defined as the current inside 8 R_E , which is the domain covered by the RCM drift physics model, while the "tail current" was taken to be everything tailward of that. The results are not sensitive to the exact separation distance.

The subsolar distance to the magnetopause is largely determined by the solar wind dynamic pressure, but the orientation and magnitude of the IMF, the time history of the solar wind, as well as internal state of the magnetosphere cause substantial scatter to the results. The Geospace model gives quite good agreement with the empirical Shue et al. (1998) model developed using a statistical database of magnetopause crossings, but the results along the magnetopause flank vary quite a bit from the empirical paraboloid shape. Especially during highly compressed situations (high dynamic pressure), the Geospace simulation gives significantly smaller distances from the Sun-Earth line to the lobe boundary than the empirical model.

425

426

427

428

429

430

431

432

433

434

435

436 437

438

439

440 441

442

443

444

445

446

447

448 449

450

451

452

453

Shukhtina et al. (2004) derived the magnetopause location using both solar wind parameters and tail magnetic flux derived from the Geoatail measurements, parametrizing the tail flaring angle. They demonstrate the strong dependence of the size of the magnetosphere on the internal state of the magnetosphere, by examining quiet periods, periods close to substorm onset, and periods of steady magnetospheric convection, which are characterized by enhanced, steady-state convection in the magnetotail, an expanded polar cap and enhanced lobe magnetic flux content (Sergeev et al., 1996).

Gordeev et al. (2015) performed an extensive comparison of global MHD simulations of the Earth's space environment using the Community Coordinated Modeling Center (CCMC) resources and four different MHD simulations, including BATSRUS, the MHD simulation core of the SWMF Geospace model used in this study. When comparing the results in that paper with our results, two things must be pointed out: (1) the Gordeev et al. (2015) study used the MHD simulations without coupling to an inner magnetosphere model, which significantly alters the "memory" of the magnetosphere, when the ring current response is not included, and (2) the comparison was made using an artificially created solar wind time series including constant solar wind and a constant IMF that flipped from B_Z northward to B_Z southward after 2 hours of northward IMF. In our case, we have simulated real events, which involve all the complexities of true solar wind driver characteristics. The Gordeev et al. (2015) study shows that the pure BATSRUS gives a subsolar location that is very highly correlated with the Shue et al. (1998) model, with even higher correlation coefficient (0.95) than that found in this study, and BATSRUS was the best-performing simulation of the four examined in that metric. They also showed that BATSRUS produces good agreement with the (Lin et al., 2010) model of the high-latitude magnetotail boundary. That model provides a more detailed description of the tail boundary including effects of the dipole tilt angle in addition to the solar wind and IMF parameters.

In conclusion, we show results from a first large statistical study of storm simulations using the SWMF Geospace model. The results help assess the usability of the geomagnetic indices, the solar wind driver functions, and point further to magnetotail parameters that could be used to define the state of the magnetosphere.

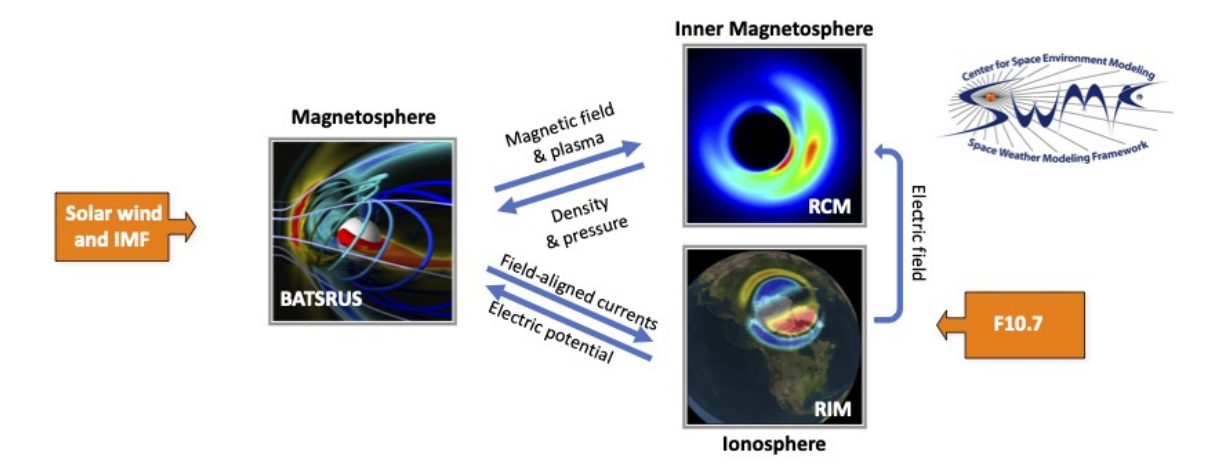


Figure 1. The SWMF Geospace model setup. The arrows indicate the two-way couplings between the modules (see text). The orange boxes indicate model input parameters.

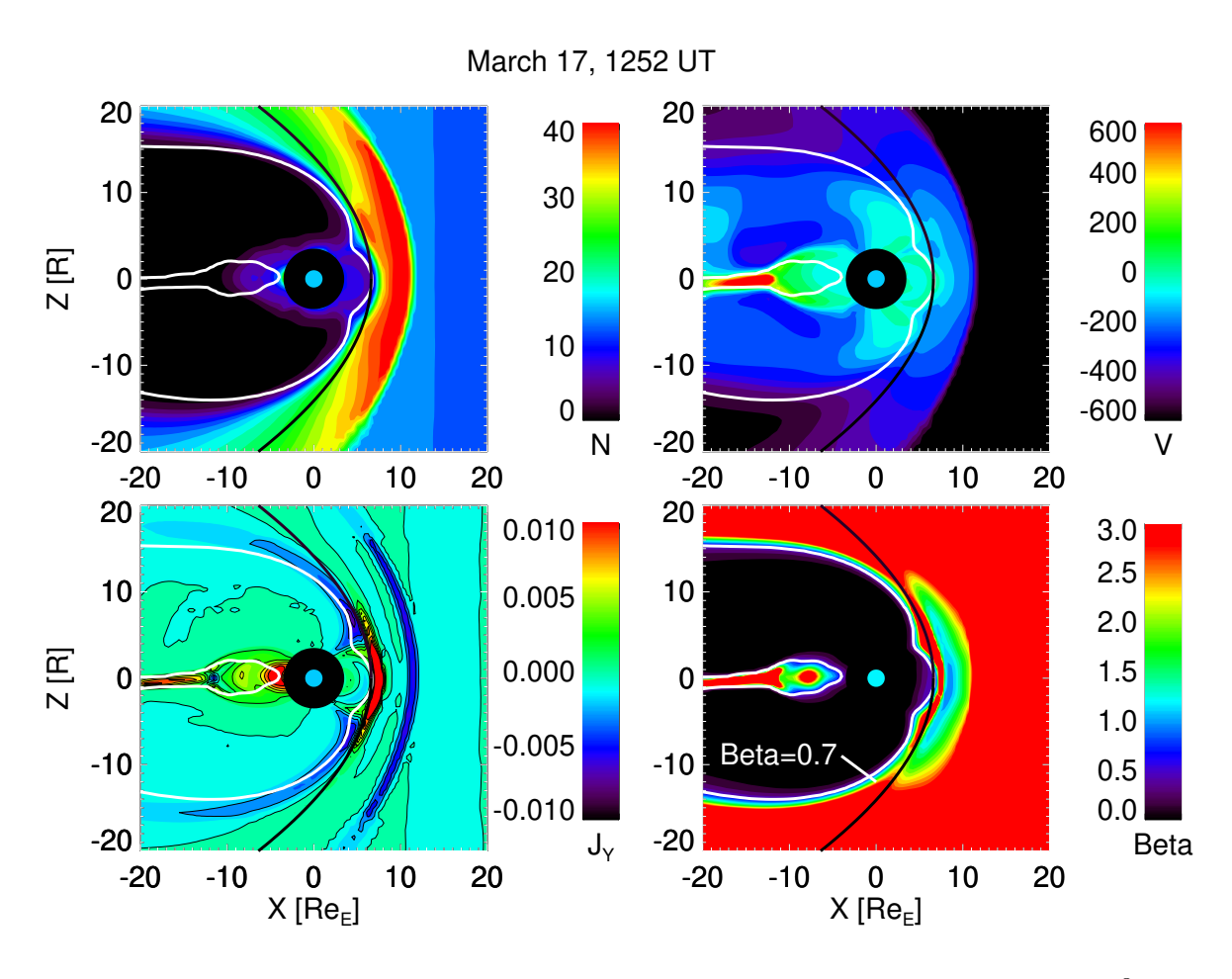


Figure 2. Noon-midnight meridian cuts from the simulation. (Top left) Plasma density in cm⁻³; (Top right) Plasma velocity V_X component in km/s; (Bottom left) Current density in μ A/m²; and (Bottom right) β^* parameter (see text). The white lines show the $\beta^*=0.7$ contours, which are used to define the simulation magnetopause location. The black thick curve shows the Shue magnetopause model (see text).

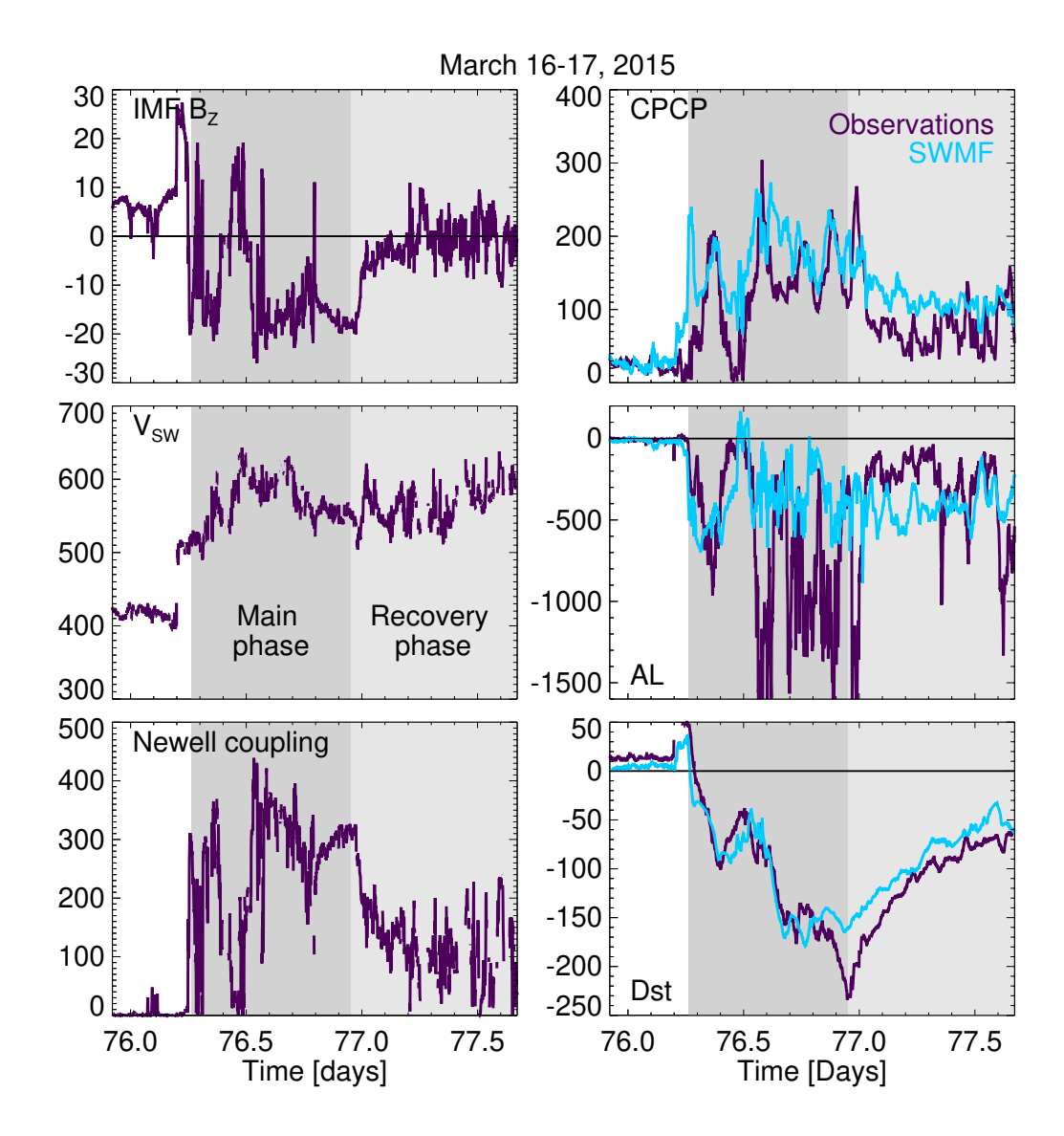


Figure 3. (Left panel) Solar wind driver parameters: (Top) IMF B_Z in nT; (Middle) solar wind speed in km/s; and (Bottom) Newell coupling function (arbitrary units, see text). (Right panel) Geomagnetic index response: (Top) Cross-polar cap potential in kV; (Middle) Auroral electrojet AL index in nT; and (Bottom) Storm Dst index in nT. The observed valueas are shown in dark blue, the SWMF simulation values in light blue. Storm main phase (from start of Dst decrease to peak Dst) and recovery phase (from peak Dst to storm end) are shown with darker and lighter gray shading, respectively.

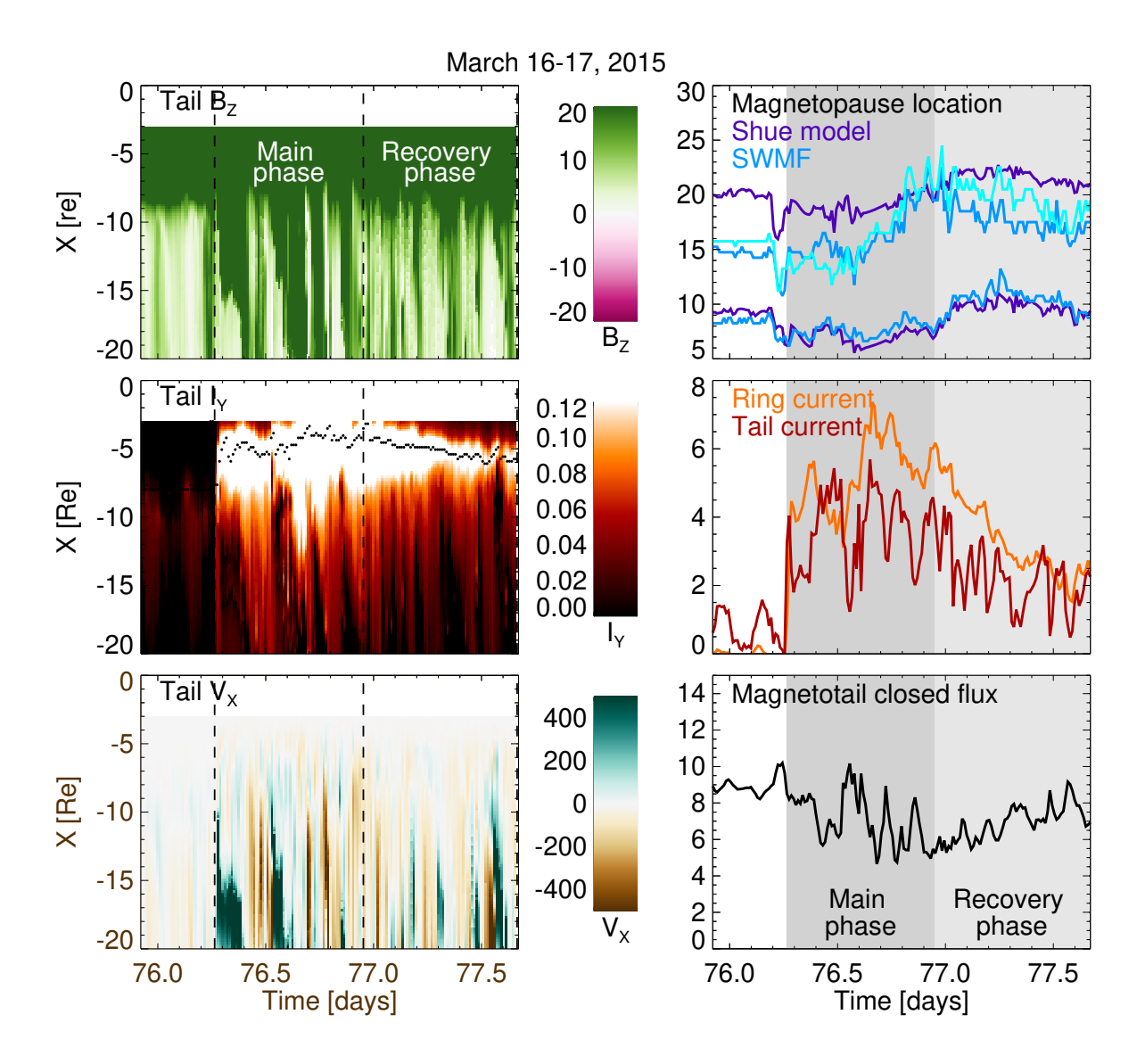


Figure 4. (Left panel) Simulation results along the magnetotail current sheet at the midnight meridian in a keogram format (see text for definition of the current sheet surface): (Top) Tail B_Z in nT; (Middle) Z-integrated current intensity (arbitrary units, see text) with current peak intensity location shown with the black dotted line; (Bottom) Plasma velocity V_X component in km/s. The storm main phase and recovery phases are defined by the dotted lines. (Right panel) Characteristic numbers for the magnetospheric state: (Top) Magnetopause nose at Y=Z=0 and magnetopause distance from the X-axis at Y=0, $X=-10R_E$. The Shue model is shown in dark blue, the SWMF Geospace values are shown in lighter blue. The southern lobe simulation value is shown with the lightest shade of blue; the Shue model is symmetric and gives the same value for northern and southern lobes. (Middle) Total ring current (orange) and tail current (dark red) integrated along the tail length in MA (see text); (Bottom) Closed magnetic flux through the magnetotail at midnight meridian (arbitrary units, see text). Storm main phase (from onset to peak Dst) and recovery phase (from peak Dst to storm end) are shown with darker and lighter gray shading, respectively.

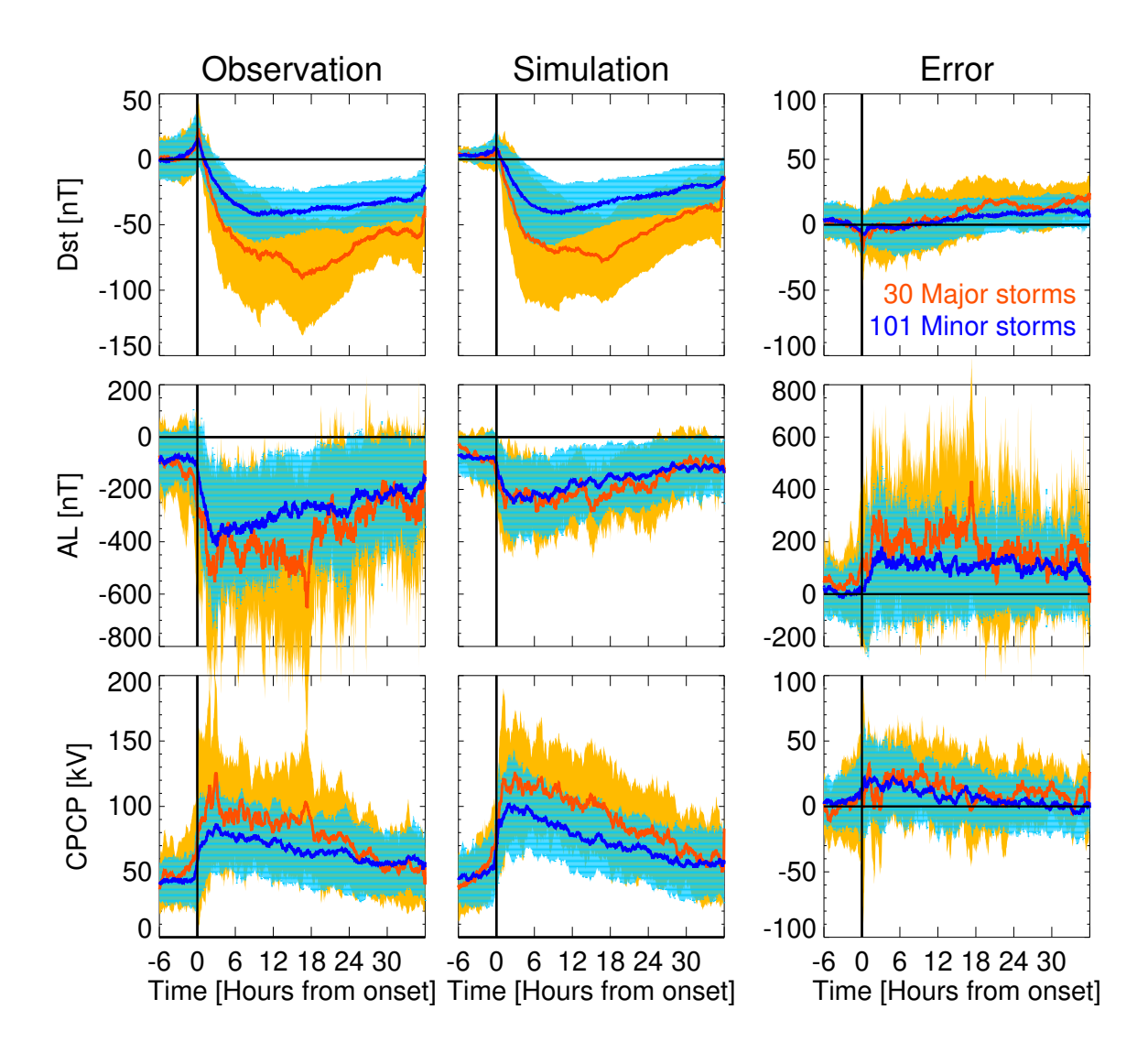


Figure 5. (Top row) Dst; (Middle row) AL; and (Bottom row) CPCP from (Left column) Observations; (Middle column) Simulation; and (Right column) Error (simulation – observation) for minor (blue, peak Dst > -100 nT) and major (red, peak Dst < -100 nT) storms. The thick solid lines show the superposed epoch curve (1-min temporal resolution), the shadings indicate the standard deviation.

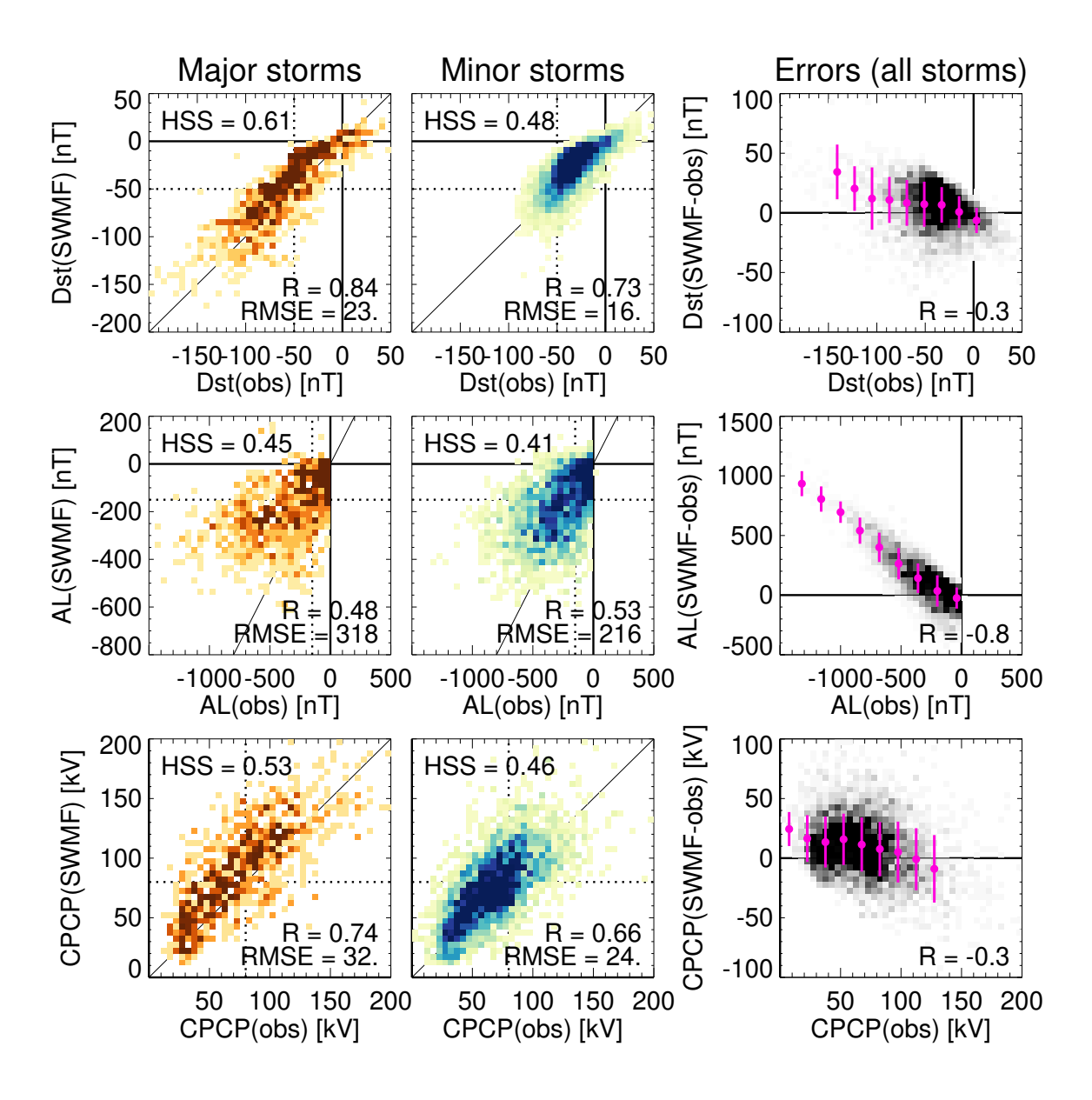


Figure 6. Heat map plots showing hourly values of (Top row) Dst; (Middle row) AL; and (Bottom row) the CPCP observed vs. simulated values, for (Right column) major storms and (Center column) minor storms. The unity line is shown in thin solid line, the dotted lines show the threshold values used in the Heidke Skill Score (HSS) calculation (see text). The heat maps indicate the share of points falling in each bin. (Right column) Errors (simulated – observed value) as function of the observed values. The magenta dots show bin averages, and the vertical thin lines indicate the standard deviation in each bin.

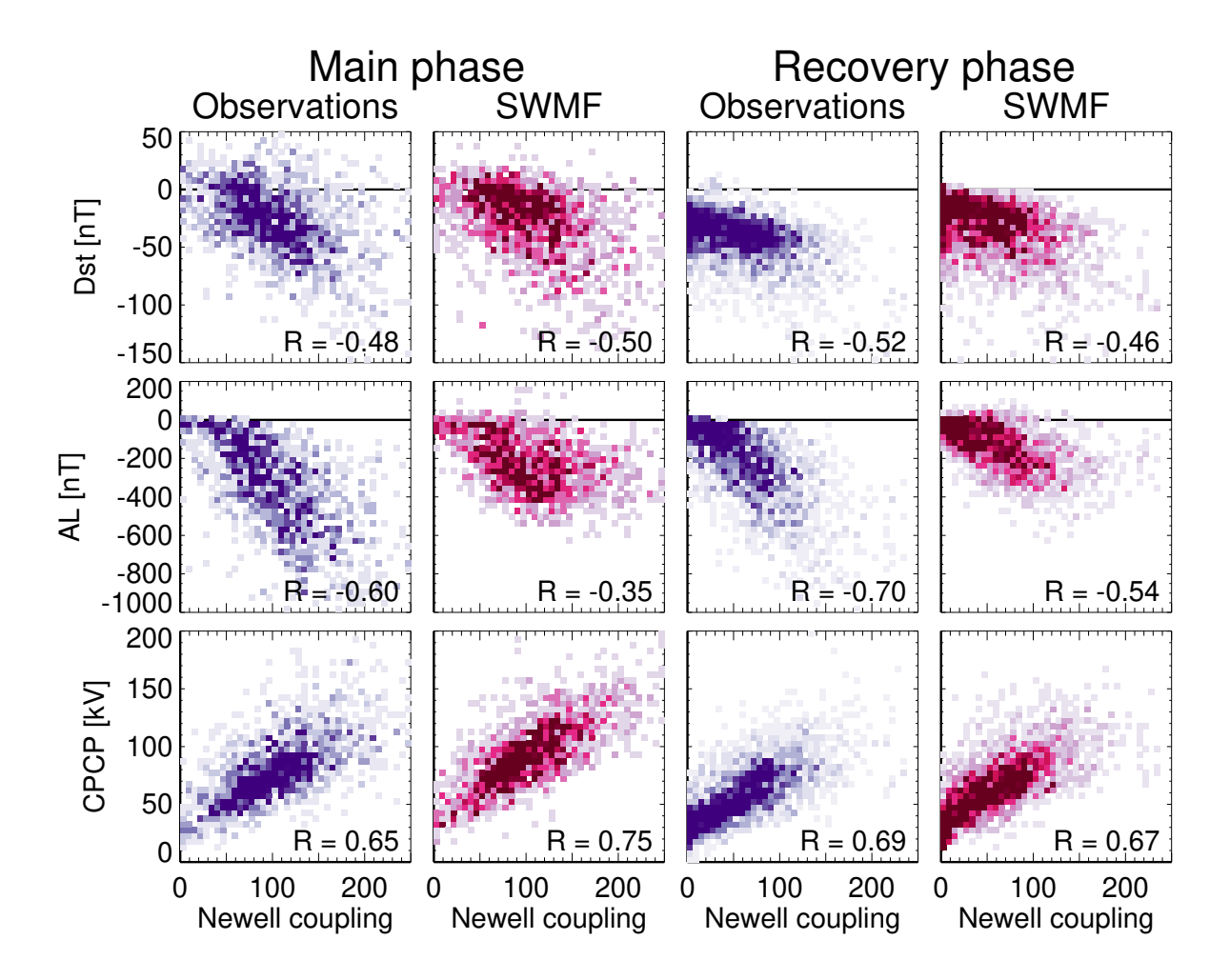


Figure 7. (Top row) Dst; (Middle row) AL; and (Bottom row) CPCP during (Left two columns) the storm main phase and (Right two columns) recovery phase as function of the Newell coupling function (in arbitrary units) using 1-hour averaged data for observations (dark purple) and simulations (dark red). The heat maps indicate the share of points falling in each bin.

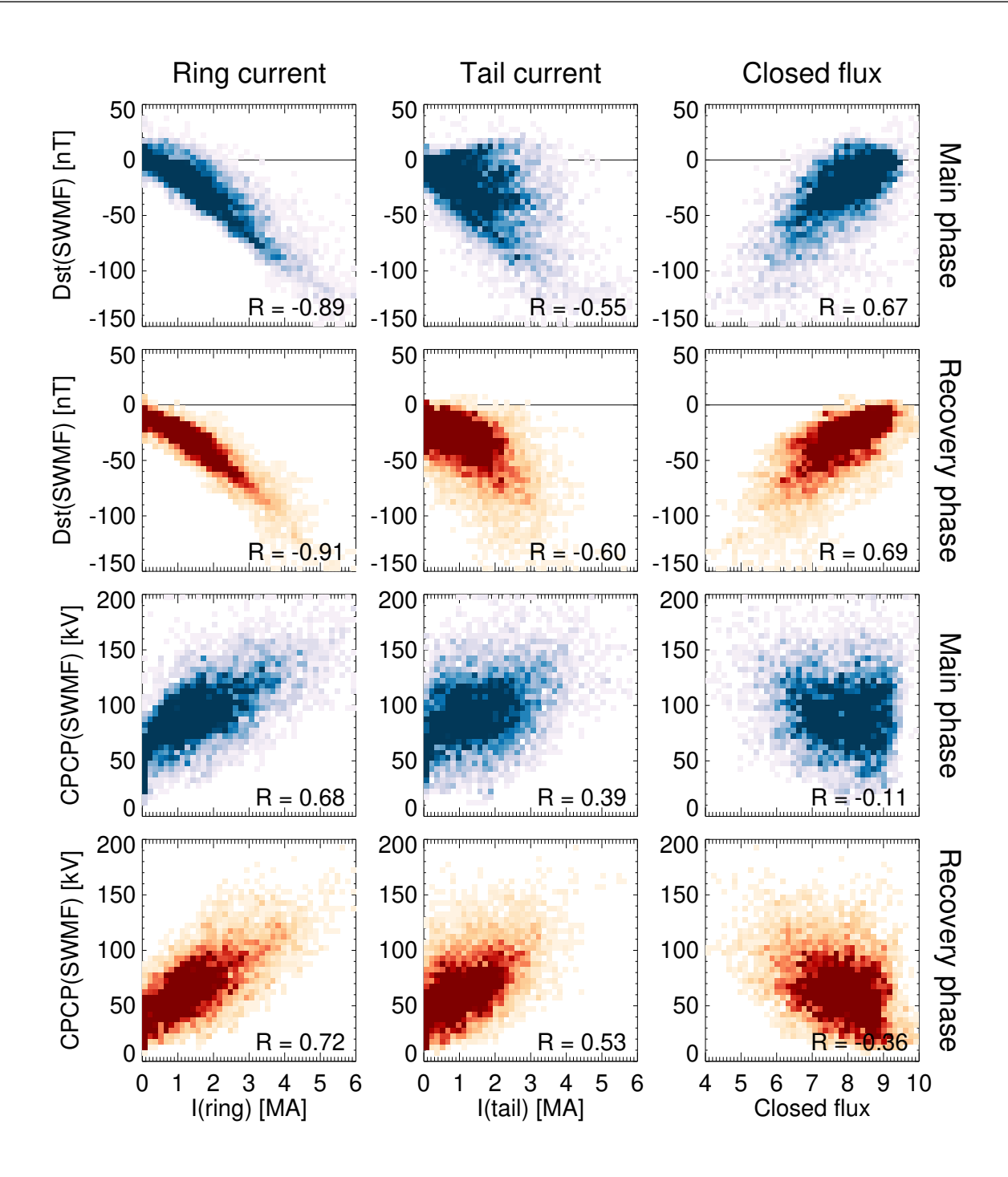


Figure 8. (Top two rows) Dst and (Bottom two rows) CPCP from the SWMF simulation as function of (Left column) total ring current; (Middle column) total tail current; and (Right column) Closed magnetic flux in the tail (see definitions given in the text). The storm main phase (blue) and recovery phase (orange) are shown separately. The data are snapshots taken at 15-min cadence in the magnetotail, tagged with the 30-min smoothed values of the indices. The heat maps indicate the share of points falling in each bin.

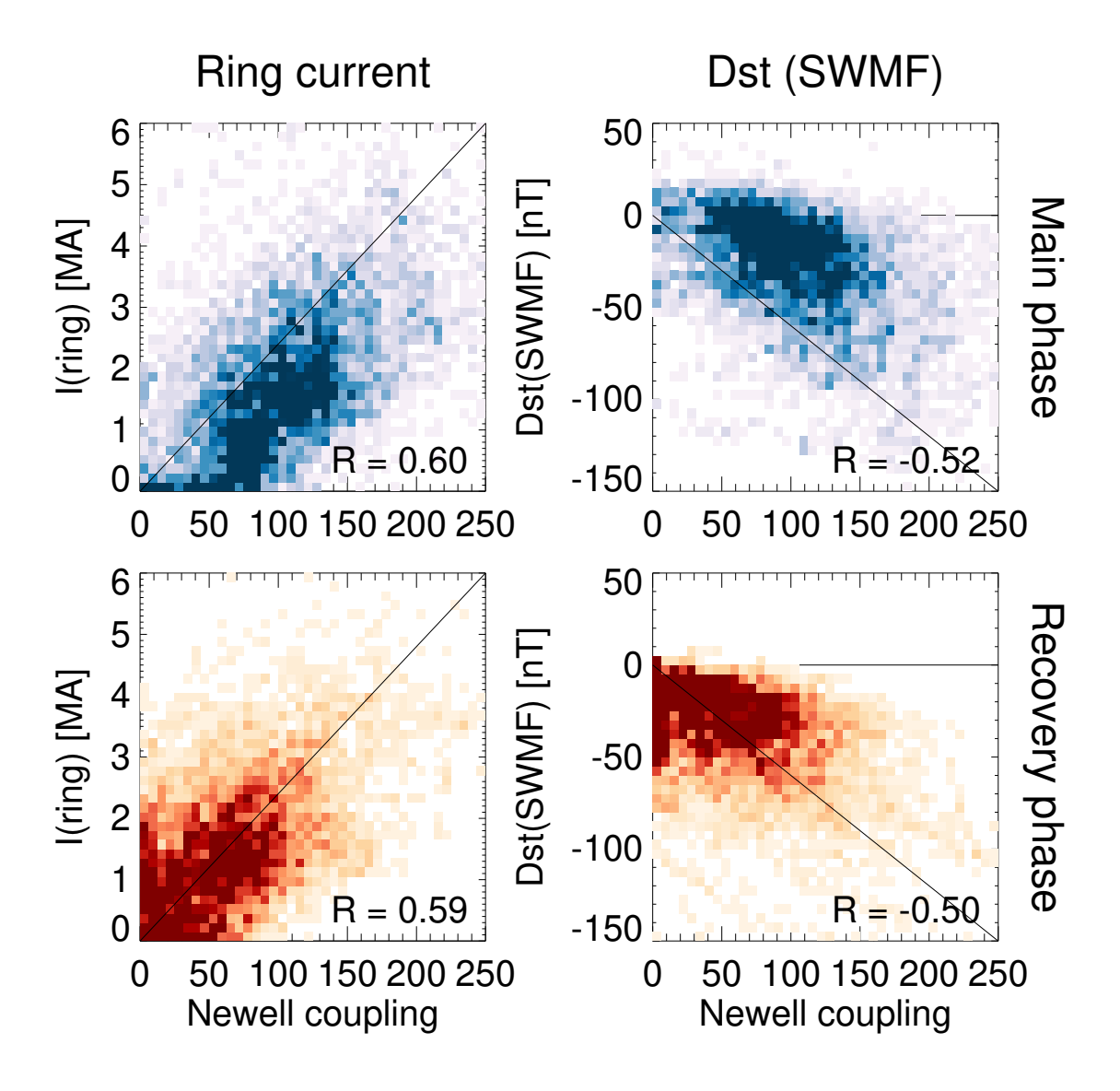


Figure 9. (Left) Total ring current and (Right) the simulation Dst during the main phase (top row) and recovery phase (bottom row) as function of Newell coupling function (in arbitrary units). The data are snapshots taken at 15-min cadence in the magnetotail, tagged with the 30-min smoothed values of the driver intensity. The heat maps indicate the share of points falling in each bin.

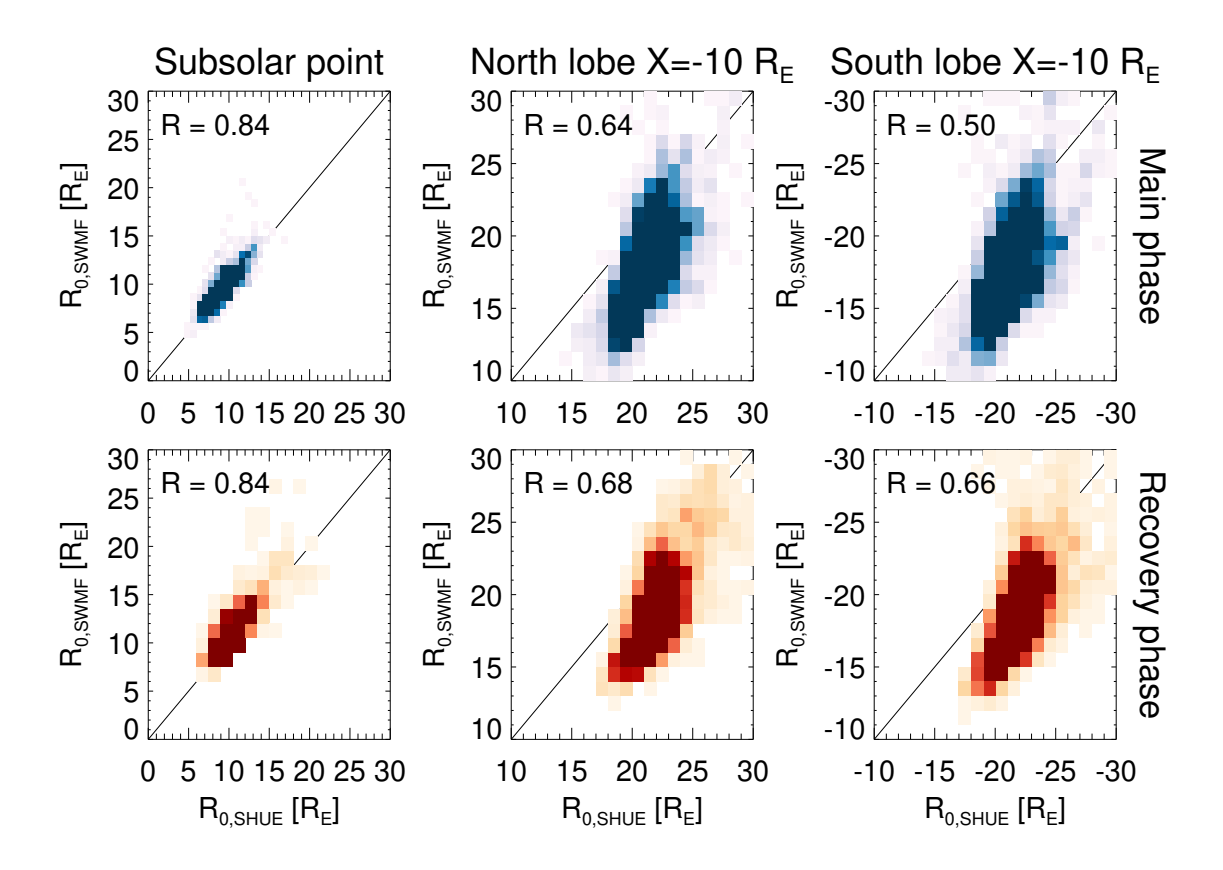


Figure 10. SWMF magnetopause location vs. the Shue model. (Left) Magnetopause subsolar position X-value for Y=Z=0. (Middle) North lobe magnetopause position Z-value at Y=0, $X=-10R_E$. (Right) South lobe magnetopause position Z-value at Y=0, $X=-10R_E$. (Top row) storm main phase, (Bottom row) storm recovery phase. The heat maps indicate the share of points falling in each bin.

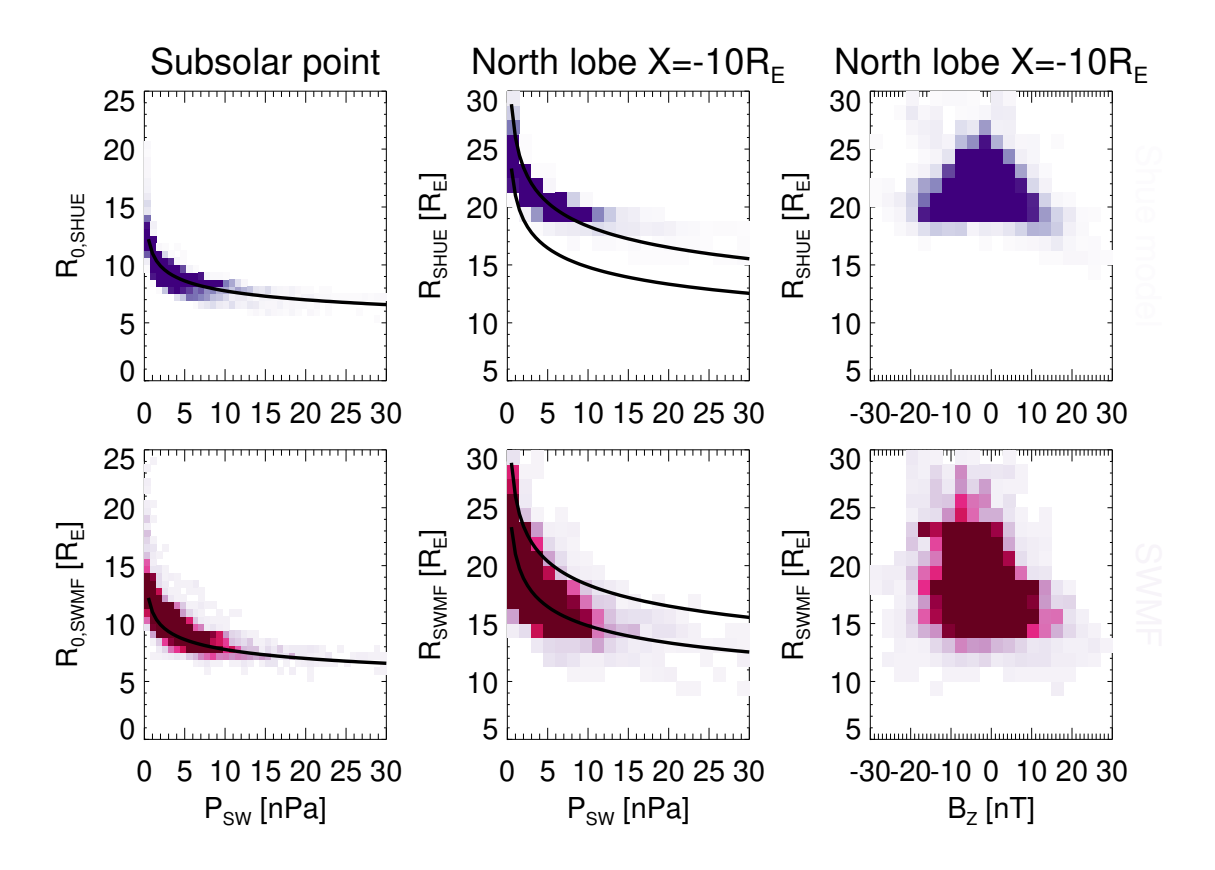


Figure 11. Magnetopause location vs solar wind driver parameters during the storm main phase. (Left) Magnetopause subsolar position X-value for Y=Z=0 as function of solar wind dynamic pressure. (Middle) North lobe magnetopause position Z-value at Y=0, $X=-10R_E$ as function of solar wind dynamic pressure. (Right) North lobe magnetopause position Z-value at Y=0, $X=-10R_E$ as function of IMF B_Z . (Top row) The Shue model values are shown in blue, (Bottom row) the SWMF values are shown in red. The black lines show the Shue model functional dependence on dynamic pressure $(P^{-1/6.6})$ using arbitrary scaling.

20100214	20120312	20130705	20150512	20160402	20181104	
20100405	20120315	20130705	20150518	20160407	20190316	١
20100411	20120315	20130709	20150607	20160412	20190510	١
20100501	20120327	20130713	20150621	20160416	20190513	
20100527	20120404	20131001	20150622	20160507	20190804	
20100803	20120422	20131008	20150704	20160604	20190830	١
20101010	20120602	20131030	20150722	20160801	20190926	
20110204	20120610	20131106	20150815	20160823		١
20110214	20120616	20131108	20150815	20161012		١
20110301	20120708	20131110	20150825	20161221		١
20110309	20120714	20131207	20150907	20170301		١
20110406	20120901	20140218	20150908	20170326		١
20110411	20120930	20140223	20150919	20170527		
20110528	20121007	20140227	20151003	20170716		
20110805	20121012	20140410	20151006	20170830		
20110909	20130116	20140507	20151018	20170906		
20110916	20130125	20140607	20151102	20170927		
20110925	20130228	20140826	20151106	20171106		١
20110926	20130317	20140912	20151130	20180318		١
20111024	20130320	20150107	20151219	20180419		
20120121	20130430	20150216	20160215	20180505		
20120124	20130517	20150316	20160216	20180531		
20120218	20130524	20150409	20160305	20180825		
20120306	20130606	20150409	20160306	20180910		
20120308	20130627	20150414	20160314	20181007		

Table 1. Storm onset dates for events used in this study. For more detailed documentation see Al Shidi et al. (2022) and the data availability statement.

CONFLICT OF INTEREST STATEMENT

The authors declare that the research was conducted in the absence of any commercial or financial relationships that could be construed as a potential conflict of interest.

AUTHOR CONTRIBUTIONS

- 460 Tuija Pulkkinen did the analysis and wrote majority of the analysis. Austin Brenner developed the methods
- and helped analyze the 2D data. Qusai Al Shidi developed methods and helped analyze the geomagnetic
- index data. Gabor Toth advised on the use of the Geospace simulation.

FUNDING

This research was funded from the NSF grant 2033563 and NASA grant 80NSSC21K1753.

ACKNOWLEDGMENTS

464 We thank the University of Michigan SWMF team for support in using the Geospace simulation.

9 APPENDIX

DATA AVAILABILITY STATEMENT

- 465 The datasets analyzed for this study can be found in the University of Michigan Deep Blue repository
- 466 under: Al Shidi, Q., Pulkkinen, T. (2022). Space Weather Modeling Framework simulations of ground
- 467 magnetometer data [Data set], University of Michigan Deep Blue Data. DOI: https://doi.org/10.7302/dkjd-
- 468 1j05 under Creative Commons license http://creativecommons.org/licenses/by/4.0/.

REFERENCES

- 469 Akasofu, S.-I. (1981). Energy coupling between the solar wind and the magnetosphere. Space Science
- 470 Reviews 28, 121–190
- 471 Al Shidi, Q., Pulkkinen, T. I., Brenner, A., Toth, G., and Gjerloev, J. (2022). Can simulations predict
- ground magnetic perturbations? Space Weather, submitted doi:10.1029
- 473 Axford, W. I. and Hines, C. O. (1961). A unifying theory of high-latitude geophysical phenomena and
- geomagnetic storms. Canadian J. Phys. 39, 1433
- 475 Borovsky, J. E. and Birn, J. (2014). The solar wind electric field does not control the dayside reconnection
- rate. Journal of Geophysical Research: Space Physics 119, 751–760. doi:https://doi.org/10.1002/
- 477 2013JA019193
- 478 Brenner, A., Pulkkinen, T. I., Al Shidi, Q., and Toth, G. (2021). Stormtime energetics: Energy transport
- across the magnetopause in a global MHD simulation. Frontiers in Astronomy and Space Sciences 8,
- 480 180. doi:10.3389/fspas.2021.756732
- 481 Burton, R. K., McPherron, R. L., and Russell, C. T. (1975). An empirical relationship between interplanetary
- 482 conditions and Dst. Journal of Geophysical Research 80, 4204
- 483 Connor, H. K., Zesta, E., Fedrizzi, M., Shi, Y., Raeder, J., Codrescu, M. V., et al. (2016). Modeling
- 484 the ionosphere-thermosphere response to a geomagnetic storm using physics-based magnetospheric
- energy input: OpenGGCM-CTIM results. Journal of Space Weather and Space Climate 6, A25.
- 486 doi:10.1051/swsc/2016019
- 487 Crooker, N. U. (1988). Mapping the merging potential from the magnetopause to the ionopause through
- 488 the dayside cusp. 93, 7338–7344. doi:10.1029/JA093iA07p07338
- 489 Daglis, I. A. (2006). Ring current dynamics. Space Sci. Rev. 124, 183-202
- 490 Davis, T. N. and Sugiura, M. (1966). Auroral electrojet activity index AE and its universal time variations.
- 491 71, 785–801. doi:10.1029/JZ071i003p00785
- 492 De Zeeuw, D., Sazykin, S., Wolf, R., Gombosi, T., Ridley, A., and Tóth, G. (2004). Coupling of a global
- MHD code and an inner magnetosphere model: Initial results 109, 219. doi:10.1029/2003JA010366
- 494 Dessler, A. J. and Parker, E. N. (1959). Hydromagnetic theory of geomagnetic storms. Journal of
- 495 Geophysical Research (1896-1977) 64, 2239–2252. doi:https://doi.org/10.1029/JZ064i012p02239
- 496 Fok, M.-C., Moore, T. E., Kozyra, J. U., Ho, G. C., and Hamilton, D. C. (1995). Three-dimensional ring
- 497 current decay model. Journal of Geophysical Research: Space Physics 100, 9619–9632. doi:https:
- 498 //doi.org/10.1029/94JA03029
- 499 Fuller-Rowell, T. J. and Evans, D. S. (1987). Height-integrated Pedersen and Hall conductivity patterns
- inferred from TIROS-NOAA satellite data. J. Geophys. Res. 92, 7606–7618
- 501 Ganushkina, N. Y., Pulkkinen, T. I., and Fritz, T. (2005). Role of substorm-associated impulsive electric
- fields in the ring current development during storms. *Annales Geophysicae* 23, 579–591. doi:10.5194/
- 503 angeo-23-579-2005

504 Gao, Y. (2012). Comparing the cross polar cap potentials measured by SuperDARN and AMIE during

- saturation intervals. Journal of Geophysical Research (Space Physics) 117, A08325. doi:10.1029/
- 506 2012JA017690
- 507 Glocer, A., Kitamura, N., Tóth, G., and Gombosi, T. (2012). Modeling solar zenith angle effects on the polar wind. *J. Geophys. Res.* 117. doi:10.1029/2011JA017136
- 509 Gombosi, T. I., Chen, Y., Glocer, A., Huang, Z., Jia, X., Liemohn, M. W., et al. (2021). What sustained
- multi-disciplinary research can achieve: The space weather modeling framework. *Journal of Space*
- 511 *Weather and Space Climate* 11, 42. doi:10.1051/swsc/2021020
- 512 Gonzalez, W. D., Joselyn, J. A., Kamide, Y., Kroehl, H. W., Rostoker, G., Tsurutani, B. T., et al. (1994).
- What is a geomagnetic storm? *Journal of Geophysical Research: Space Physics* 99, 5771–5792.
- 514 doi:https://doi.org/10.1029/93JA02867
- 515 Gordeev, E., Sergeev, V., Honkonen, I., Kuznetsova, M., Rastätter, L., Palmroth, M., et al. (2015). Assessing
- the performance of community-available global mhd models using key system parameters and empirical
- relationships. *Space Weather* 13, 868–884. doi:https://doi.org/10.1002/2015SW001307
- 518 Hairston, M. R., Heelis, R. A., and Rich, F. J. (1998). Analysis of the ionospheric cross polar cap potential
- drop using DMSP data during the National Space Weather Program study period. 103, 26337–26348.
- 520 doi:10.1029/97JA03241
- 521 Heidke, P. (1926). Berechnung des erfolges und der gute der windstarkevorhersagen im
- sturmwarnungsdienst. Geogr. Ann. 8, 301–349
- 523 Hu, Y.-Q., Guo, X.-C., Li, G.-Q., Wang, C., and Huang, Z.-H. (2005). Oscillation of Quasi-Steady Earth's
- 524 Magnetosphere. Chinese Physics Letters 22, 2723–2726. doi:10.1088/0256-307X/22/10/073
- 525 Häkkinen, L. V. T., Pulkkinen, T. I., Nevanlinna, H., Pirjola, R. J., and Tanskanen, E. I. (2002). Effects
- of induced currents on dst and on magnetic variations at midlatitude stations. *Journal of Geophysical*
- 527 Research: Space Physics 107, SMP 7–1–SMP 7–8. doi:10.1029/2001JA900130
- 528 Iijima, T. and Potemra, T. A. (1976). The amplitude distribution of field-aligned currents at northern high
- latitudes observed by Triad. J. Geophys. Res. 81, 2165
- 530 Janhunen, P., Palmroth, M., Laitinen, T., Honkonen, I., Juusola, L., and Facskó, T. I., G.and Pulkkinen
- 531 (2012). The GUMICS-4 global MHD magnetosphere-ionosphere coupling simulation. *Journal of*
- 532 Atmospheric and Solar-Terrestrial Physics 80, 48–59
- 533 Jordanova, V. K., Farrugia, C. J., Thorne, R. M., Khazanov, G. V., Reeves, G. D., and Thomsen, M. F.
- 534 (2001). Modeling ring current proton precipitation by electromagnetic ion cyclotron waves during
- the may 14–16, 1997, storm. *Journal of Geophysical Research: Space Physics* 106, 7–22. doi:https:
- 536 //doi.org/10.1029/2000JA002008
- 537 Kalegaev, V. V. and Makarenkov, E. V. (2008). Relative importance of ring and tail currents to Dst under
- extremely disturbed conditions. *Journal of Atmospheric and Solar-Terrestrial Physics* 70, 519–525.
- 539 doi:10.1016/j.jastp.2007.08.029
- 540 Kilpua, E., Koskinen, H. E. J., and Pulkkinen, T. I. (2017). Coronal mass ejections and their sheath regions
- in interplanetary space. Living Reviews in Solar Physics 14, 5. doi:10.1007/s41116-017-0009-6
- 542 Koustov, A. V., Khachikjan, G. Y., Makarevich, R. A., and Bryant, C. (2009). On the SuperDARN
- cross polar cap potential saturation effect. Annales Geophysicae 27, 3755–3764. doi:10.5194/
- 544 angeo-27-3755-2009
- 545 Kwagala, N. K., Hesse, M., Moretto, T., Tenfjord, P., Norgren, C., Tóth, G., et al. (2020). Validating the
- Space Weather Modeling Framework (SWMF) for applications in northern Europe. Ground magnetic
- perturbation validation. Journal of Space Weather and Space Climate 10, 33. doi:10.1051/swsc/2020034

Lakka, A., Pulkkinen, T. I., Dimmock, A. P., Myllys, M., Honkonen, I., and Palmroth, M. (2018). The

- 549 Cross-Polar Cap Saturation in GUMICS-4 During High Solar Wind Driving. *Journal of Geophysical*
- 550 Research (Space Physics) 123, 3320–3332. doi:10.1002/2017JA025054
- 551 Liemohn, M., Ganushkina, N., De Zeeuw, D., Rastaetter, L., Kuznetsova, M., Welling, D., et al. (2018).
- Real-time swmf at ccmc: assessing the dst output from continuous operational simulations. *Space*
- 553 Weather 16, 1583. doi:10.1029/2018SW001953
- Liemohn, M. W., Kozyra, J. U., Clauer, C. R., Khazanov, G. V., and Thomsen, M. F. (2002). Adiabatic
- energization in the ring current and its relation to other source and loss terms. *J. Geophys. Res.* 107.
- 556 doi:10.1029/2001JA000243
- 557 Liemohn, M. W., McCollough, J. P., Jordanova, V. K., Ngwira, C. M., Morley, S. K., Cid, C., et al.
- 558 (2018). Model Evaluation Guidelines for Geomagnetic Index Predictions. *Space Weather* 16, 2079–2102.
- 559 doi:10.1029/2018SW002067
- 560 Lin, R. L., Zhang, X. X., Liu, S. Q., Wang, Y. L., and Gong, J. C. (2010). A three-dimensional
- asymmetric magnetopause model. *Journal of Geophysical Research: Space Physics* 115. doi:https:
- 562 //doi.org/10.1029/2009JA014235
- 563 Lockwood, M. (2019). Does adding solar wind poynting flux improve the optimum solar wind-
- magnetosphere coupling function? *Journal of Geophysical Research: Space Physics* 124, 5498–5515.
- doi:https://doi.org/10.1029/2019JA026639
- 566 Lockwood, M. (2022). Solar wind—magnetosphere coupling functions: Pitfalls, limitations, and
- 567 applications. *Space Weather* 20, e2021SW002989. doi:https://doi.org/10.1029/2021SW002989.
- 568 E2021SW002989 2021SW002989
- 569 Lockwood, M., Hairston, M., Finch, I., and Rouillard, A. (2009). Transpolar voltage and polar cap flux
- 570 during the substorm cycle and steady convection events. Journal of Geophysical Research (Space
- 571 *Physics*) 114, A01210. doi:10.1029/2008JA013697
- 572 Lockwood, M. and McWilliams, K. A. (2021). On optimum solar wind-magnetosphere coupling
- 573 functions for transpolar voltage and planetary geomagnetic activity. *Journal of Geophysical Research:*
- 574 Space Physics 126, e2021JA029946. doi:https://doi.org/10.1029/2021JA029946. E2021JA029946
- 575 2021JA029946
- 576 Lopez, R. E., Bruntz, R., Mitchell, E. J., Wiltberger, M., Lyon, J. G., and Merkin, V. G. (2010). Role of
- 577 magnetosheath force balance in regulating the dayside reconnection potential. *Journal of Geophysical*
- 578 Research 115, 216. doi:10.1029/2009JA014597
- 579 Maimaiti, M., Kunduri, B., Ruohoniemi, J. M., Baker, J. B. H., and House, L. L. (2019). A deep
- learning-based approach to forecast the onset of magnetic substorms. *Space Weather* 17, 1534–1552.
- 581 doi:https://doi.org/10.1029/2019SW002251
- 582 McPherron, R. L., Hsu, T.-S., and Chu, X. (2015). An optimum solar wind coupling function for the al
- index. Journal of Geophysical Research: Space Physics 120, 2494–2515. doi:https://doi.org/10.1002/
- 584 2014JA020619
- 585 Milan, S. E., Lester, M., Cowley, S. W. H., Oksavik, K., Brittnacher, M., Greenwald, R. A., et al. (2003).
- Variations in the polar cap area during two substorm cycles. *Annales Geophysicae* 21, 1121–1140.
- 587 doi:10.5194/angeo-21-1121-2003
- 588 Mukhopadhyay, A., Welling, D., Liemohn, M., Ridley, A., Burleigh, M., Wu, C., et al. (2022). Global
- driving of auroral precipitation: 1. balance of sources. *Journal of Geophysical Research: Space Physics*
- 590 127, e2022JA030323. doi:https://doi.org/10.1029/2022JA030323. E2022JA030323 2022JA030323
- 591 Mukhopadhyay, A., Welling, D. T., Liemohn, M. W., Ridley, A. J., Chakraborty, S., and Anderson, B. J.
- 592 (2020). Conductance model for extreme events: Impact of auroral conductance on space weather forecasts.

593 Space Weather 18, e2020SW002551. doi:https://doi.org/10.1029/2020SW002551. E2020SW002551

- 594 10.1029/2020SW002551
- 595 Myllys, M., Kilpua, E. K. J., and Lavraud, B. (2017). Interplay of solar wind parameters and physical
- 596 mechanisms producing the saturation of the cross polar cap potential. *Geophysical Research Letters* 44,
- 597 3019–3027. doi:10.1002/2017GL072676
- 598 Newell, P., Liou, K., Gjerloev, J., Sotirelis, T., Wing, S., and Mitchell, E. (2016). Substorm probabilities
- are best predicted from solar wind speed. Journal of Atmospheric and Solar-Terrestrial Physics 146,
- 600 28–37. doi:https://doi.org/10.1016/j.jastp.2016.04.019
- 601 Newell, P. T., Sotirelis, T., Liou, K., Meng, C. I., and Rich, F. J. (2007). A nearly universal solar
- wind-magnetosphere coupling function inferred from 10 magnetospheric state variables. *Journal of*
- 603 Geophysical Research 112, 01206
- Newell, P. T., Sotirelis, T., and Wing, S. (2009). Diffuse, monoenergetic, and broadband aurora: The global
- precipitation budget. Journal of Geophysical Research (Space Physics) 114, A09207. doi:10.1029/
- 606 2009JA014326
- Palmroth, M., Laitinen, T., and Pulkkinen, T. I. (2006). Magnetopause energy and mass transfer: results
- from a global MHD simulation. Annales Geophysicae, 1–14
- 609 Palmroth, M., Pulkkinen, T. I., Janhunen, P., and Wu, C.-C. (2003). Stormtime energy transfer in global
- 610 MHD simulation. Journal of Geophysical Research 108, 1048. doi:01029/2002JA009446
- 611 Papitashvili, N., Bilitza, D., and King, J. (2014). OMNI: A Description of Near-Earth Solar Wind
- Environment. In 40th COSPAR Scientific Assembly. vol. 40, C0.1–12–14
- 613 Powell, K. G., Roe, P. L., Linde, T. J., Gombosi, T. I., and De Zeeuw, D. L. (1999). A Solution-Adaptive
- 614 Upwind Scheme for Ideal Magnetohydrodynamics. Journal of Computational Physics 154, 284–309.
- 615 doi:10.1006/jcph.1999.6299
- 616 Pulkkinen, A., Rastatter, L., Kuznetova, M., Singer, H., Balch, C., Weimer, D., et al. (2013). Community-
- wide validation of geospace model ground magnetic field perturbation predictions to support model
- transition to operations. Space Weather 11, 369–385. doi:10.1002/swe.20056
- 619 Pulkkinen, T., Palmroth, M., and Laitinen, T. (2008). Energy as a tracer of magnetospheric processes:
- 620 GUMICS-4 global MHD results and observations compared. Journal of Atmospheric and Solar-
- 621 *Terrestrial Physics* 70, 687–707
- 622 Pulkkinen, T. I., Dimmock, A. P., Lakka, A., Osmane, A., Kilpua, E., Myllys, M., et al. (2016).
- Magnetosheath control of solar wind-magnetosphere coupling efficiency. Journal of Geophysical
- 624 Research (Space Physics) 121, 8728–8739. doi:10.1002/2016JA023011
- Pulkkinen, T. I., Ganushkina, N. Y., Tanskanen, E. I., Kubyshkina, M., Reeves, G. D., Thomsen, M. F., et al.
- 626 (2006a). Magnetospheric current systems during stormtime sawtooth events. *Journal of Geophysical*
- 627 *Research* 111
- 628 Pulkkinen, T. I., Palmroth, M., Tanskanen, E. I., Janhunen, P., Koskinen, H. E. J., and Laitinen, T. V.
- 629 (2006b). New interpretation of magnetospheric energy circulation. Geophysical Research Letters 33
- 630 Ridley, A., Gombosi, T., and De Zeeuw, D. L. (2004). Ionospheric control of the magnetospheric
- configuration: Conductance. Ann. Geophys. 22, 567–584
- 632 Ridley, A., Gombosi, T., and Dezeeuw, D. (2004). Ionospheric control of the magnetosphere: conductance.
- 633 Annales Geophysicae 22, 567–584. doi:10.5194/angeo-22-567-2004
- Russell, C. T., Luhmann, J. G., and Lu, G. (2001). Nonlinear response of the polar ionosphere to large
- values of the interplanetary electric field. 106, 18495–18504. doi:10.1029/2001JA900053
- 636 Sergeev, V., Pellinen, R. J., and Pulkkinen, T. I. (1996). Steady magnetospheric convection: A review of
- recent results. Space Sci. Rev. 75, 551–604

638 Shue, J.-H., Chao, J. K., Fu, H. C., Russell, C. T., Song, P., Khurana, K. K., et al. (1997). A new functional

- form to study the solar wind control of the magnetopause size and shape. *Journal of Geophysical*
- 640 Research 102, 9497
- 641 Shue, J.-H., Chao, J. K., Fu, H. C., Russell, C. T., Song, P., Khurana, K. K., et al. (1998). Magnetopause
- location under extreme solar wind conditions. *Journal of Geophysical Research* 103, 17691–17700.
- 643 doi:10.1029/98JA01103
- 644 Shukhtina, M. A., Dmitrieva, N. P., and Sergeev, V. A. (2004). Quantitative magnetotail
- characteristics of different magnetospheric states. *Annales Geophysicae* 22, 1019–1032. doi:10.5194/
- 646 angeo-22-1019-2004
- 647 Siscoe, G. L., Erickson, G. M., Sonnerup, B. U. Ö., Maynard, N. C., Schoendorf, J. A., Siebert, K. D., et al.
- 648 (2002). Hill model of transpolar potential saturation: Comparisons with MHD simulations. *Journal of*
- 649 Geophysical Research (Space Physics) 107, 1075. doi:10.1029/2001JA000109
- 650 Tanskanen, E. I., Viljanen, A., Pulkkinen, T. I., Pirjola, R., Häkkinen, L., Pulkkinen, A., et al. (2001). At
- substorm onset, 40% of al comes from underground. *Journal of Geophysical Research: Space Physics*
- 652 106, 13119–13134. doi:10.1029/2000JA900135
- 653 Toffoletto, F., Sazykin, S., Spiro, R., and Wolf, R. (2003). Inner magnetospheric modeling with the Rice
- 654 Convection Model. Space Sci Rev. 107, 175–196. doi:10.1023/A:1025532008047
- 655 Tóth, G., van der Holst, B., Sokolov, I. V., De Zeeuw, D. L., Gombosi, T. I., Fang, F., et al. (2012).
- Adaptive numerical algorithms in space weather modeling. Journal of Computational Physics 231,
- 657 870–903. doi:10.1016/j.jcp.2011.02.006
- 658 Troshichev, O., Shishkina, E., Meng, C.-I., and Newell, P. (1996). Identification of the poleward boundary
- of the auroral oval using characteristics of ion precipitation. J. Geophys. Res. 101, 5035
- 660 Tsyganenko, N. A. and Sitnov, M. I. (2005). Modeling the dynamics of the inner magnetosphere
- during strong geomagnetic storms. Journal of Geophysical Research (Space Physics) 110, A03208.
- doi:10.1029/2004JA010798
- Vasyliunas, V. M. (1970). Mathematical models of magnetospheric convection and its coupling to the
- 664 ionosphere. In Particles and fields in the magnetosphere, ed. B. M. McCormack (Dordrecht, Holland).
- 665 60–71
- 666 Wang, C., Han, J. P., Li, H., Peng, Z., and Richardson, J. D. (2014). Solar wind-magnetosphere energy
- 667 coupling function fitting: Results from a global mhd simulation. *Journal of Geophysical Research*:
- 668 Space Physics 119, 6199–6212. doi:https://doi.org/10.1002/2014JA019834
- 669 Wolf, R. A. (1983). Computer Model of Inner Magnetospheric Convection. In Solar-Terrestrial Physics:
- 670 Principles and Theoretical Foundations, eds. R. L. Carovillano and J. M. Forbes. vol. 104 of Astrophysics
- *and Space Science Library*, 342. doi:10.1007/978-94-009-7194-3_14
- 672 Yu, Y. and Ridley, A. (2008). Validation of the Space Weather Modeling Framework using ground-based
- 673 magnetometers. *Space Weather* 6. doi:10.1029/2007SW000345
- Yue, C., Jun, C.-W., Bortnik, J., An, X., Ma, Q., Reeves, G. D., et al. (2019). The relationship between
- emic wave properties and proton distributions based on van allen probes observations. *Geophysical*
- 676 Research Letters 46, 4070–4078. doi:https://doi.org/10.1029/2019GL082633